

See discussions, stats, and author profiles for this publication at: <https://www.researchgate.net/publication/256427005>

# Evaluation of Mesostructure of Particulate Composites by Quantitative Stereology and Random Sequential Packing Model of Mono-/Polydisperse Convex Polyhedral Particles

ARTICLE *in* INDUSTRIAL & ENGINEERING CHEMISTRY RESEARCH · MAY 2013

Impact Factor: 2.59 · DOI: 10.1021/ie3025449

---

CITATIONS

11

READS

76

## 3 AUTHORS:



W. Xu

Hohai University

25 PUBLICATIONS 193 CITATIONS

[SEE PROFILE](#)



Huisu Chen

Southeast University (China)

85 PUBLICATIONS 533 CITATIONS

[SEE PROFILE](#)



Lin Liu

Hohai University

18 PUBLICATIONS 72 CITATIONS

[SEE PROFILE](#)

# Evaluation of Mesostructure of Particulate Composites by Quantitative Stereology and Random Sequential Packing Model of Mono-/Polydisperse Convex Polyhedral Particles

Wenxiang Xu,<sup>†,‡</sup> Huisu Chen,<sup>\*,†</sup> and Lin Liu<sup>§</sup>

<sup>†</sup>Jiangsu Key Laboratory of Construction Materials, School of Materials Science and Engineering, Southeast University, Nanjing 211189, China

<sup>‡</sup>Institute of Soft Matter Mechanics, College of Mechanics and Materials, Hohai University, Nanjing 210098, China

<sup>§</sup>College of Civil and Transportation Engineering, Hohai University, Nanjing 210098, China

**ABSTRACT:** Random packing of particles has served as a topic of intense research in the chemical, physical, engineering, and material fields. The majority of previous works focused on the random packing models of spherical, cylindrical, and ellipsoidal particles, whereas little is known about polyhedral particles. In this article, a modeling study of the random packing of convex polyhedral particles is presented in detail, using an interparticle contact detection algorithm, a particle-to-container wall intersection detection algorithm, and a random sequential packing algorithm for hard particles, and the accuracy and efficiency of the contact detection algorithm are compared with those of methods from the literature. With the random packing model and a specified particle size distribution, mesostructure models of particulate composites with mono-/polydisperse particles were generated and validated by a sectioning analysis algorithm. Based on quantitative stereological theories and the sectioning analysis algorithm, the effects of particle shape on the mesostructures composed of the monodisperse and polydisperse particles were evaluated. Further, the statistical results were verified by validation against experimental results from the literature and theoretical results.

## 1. INTRODUCTION

At the mesoscopic scale, particulate composites, such as ceramics, glass, colloidal materials, polymer blends, and cementitious materials, are composed of randomly packed particles with irregular geometrical shapes. The evolution of the interior structure of a particulate composite is, to some extent, dependent on its initial random packing structure. Also, the random packing of particles can provide insight into the effects of various characteristic parameters (e.g., particle size, shape, gradation, distribution) on the characteristics of the interfacial transition zones (ITZs),<sup>1,2</sup> porous structure,<sup>3–5</sup> and macroscopic physical properties such as transport and mechanical properties.<sup>6–8</sup>

For the design of high-performance particulate composites, insight into the mesostructures of particulate composites and their relationship to the properties of the same particulate composites are of paramount importance. Nonetheless, opaque materials such as particulate composites do not allow easy access to the three-dimensional (3D) mesostructure. Generally speaking, conventional experimental work is laborious and involves relatively large errors and uncertainties.<sup>9</sup> Through the application of digital image analysis, the mesostructures of particulate composites have been broadly investigated,<sup>10–12</sup> with particles of arbitrary geometrical shapes represented by pixels for two-dimensional (2D) images or voxels for 3D images. However, the accuracy of digital image models is limited by the image resolution of the equipment.<sup>13–15</sup>

To overcome these difficulties, various random packing models of particles have been developed to facilitate the determination of the mesostructure of particulate composites, for example, the random sequential packing model,<sup>16–18</sup> discrete element model (DEM),<sup>19–24</sup> molecular dynamics model (MDM),<sup>25–28</sup>

relaxation iteration model,<sup>29–31</sup> mechanical contraction model,<sup>32,33</sup> simulated annealing model,<sup>34,35</sup> compactness and selection model,<sup>36</sup> and particle suspension model.<sup>37</sup> Most of these models consider spheres, ellipsoids, or spherocylinders in 2D or 3D space. Actually, in particulate composites, realistic particles rarely have perfect spherical or ellipsoidal shapes. Instead, they might have corner angles and facets. Recently, Torquato and Jiao<sup>38,39</sup> presented a random packing model of monodisperse Platonic and Archimedean particles (which are essentially convex polyhedra) utilizing a so-called adaptive shrinking cell scheme. Similar experimental and modeling studies have also been introduced by others.<sup>40–42</sup> However, as polydisperse systems, the common characteristic of particulate composites with random distributions of large numbers of particles is that the particles satisfy a specified probability distribution model. To date, it is not clear how to simulate the random packing models of monodisperse convex polyhedral particles or polydisperse convex polyhedral particles with a specified particle size distribution. Furthermore, for such particle packing models representing the mesostructure of particulate composites, accessing the mesostructure information is still difficult. It is our intention in the present work to address this gap.

This article attempts to present random packing models of mono-/polydisperse convex polyhedral particles satisfying specific probability distribution models that can be used to construct the mesostructure of the particulate composites,

**Received:** September 18, 2012

**Revised:** February 26, 2013

**Accepted:** April 9, 2013

**Published:** April 9, 2013

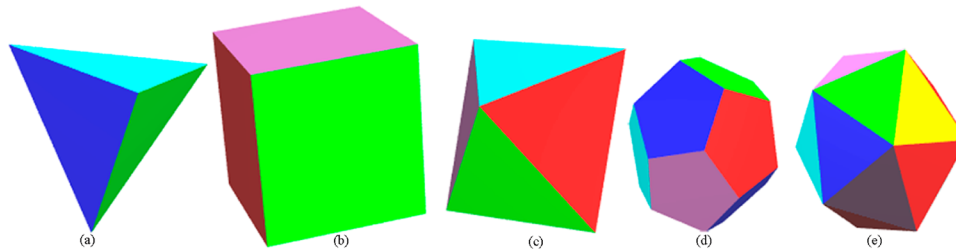


**Figure 1.** Realizations of Platonic particles: (a) tetrahedron, (b) cube, (c) octahedron, (d) dodecahedron, and (e) icosahedron.

including an interparticle contact detection algorithm, a particle-to-container wall intersection detection algorithm, and a random sequential packing algorithm. The shapes of particles are considered as Platonic solids. In addition, to validate the reliability of the particle packing models and to access the mesostructure information, a sectioning analysis algorithm is elaborated in this work. Notably, the proposed algorithms can be used to realize and characterize not only mesoscopic convex polyhedral particle packing structures but also microscopic and macroscopic convex polyhedral particle packing structures.

The remainder of this article is outlined as follows: In section 2, the geometrical models of the Platonic particles for the modeling study are introduced. In section 3, a numerical algorithm is illustrated to detect contact between convex polyhedra in detail. In section 4, a random sequential packing algorithm and a particle-to-container wall intersection detection algorithm are elaborated. In section 5, the mesostructure models of particulate composites composed of mono-/polydisperse Platonic particles are constructed and quantitatively investigated by applying stereological tools and a sectioning analysis algorithm. The final section presents our conclusions.

## 2. GEOMETRICAL MODELS OF PLATONIC PARTICLES

Platonic particles are convex polyhedra with faces composed of congruent convex regular polygons. There are five such types of particles: tetrahedron, cube, octahedron, dodecahedron, and icosahedron (see Figure 1).

Generally, a convex polyhedron is the convex hull of its vertices. Similarly, the set of vertices of a Platonic particle can be used as a useful geometrical representation of such a particle. It is convenient to choose the origin of the local coordinate system for the vertices to be the centroid  $C(x_0, y_0, z_0)$  of the Platonic particle. Other important geometrical properties of the Platonic particle, such as its faces and edges, can be represented as certain subsets of the vertices. As the Platonic particles are highly symmetric, their vertices, edges, and faces can be derived by a given size parameter, such as the length of a side or the radius of the circumscribed sphere (as described in more detail in Appendix A). In other words, Platonic particles can be characterized by just a size parameter. However, in the random packing model of particles, particles are usually generated randomly in a global coordinate system. Such randomly generated particles exhibit position and orientation sensitivities in the global coordinate system. Therefore, it is necessary to introduce generalized geometrical models that can represent Platonic particles with arbitrary positions and orientations.

As an introductory example, an icosahedron has 20 vertices  $P_v$  ( $v = 1, \dots, 20$ ) (see Appendix A), and its centroid  $C$  is obtained by generating a random point that reflects the random position of the icosahedron in the global coordinate system  $O-XYZ$ . First, the global coordinate system  $O-XYZ$  is translated to a local

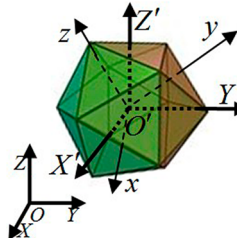


**Figure 2.** Realization of linear transformation of the global coordinate system  $O-XYZ$ .

coordinate system  $O'-X'Y'Z'$  (see Figure 2), so that the origin  $O'$  of the local coordinate system is located at the centroid  $C$ , and the translational matrix  $T$  is given by

$$T = \begin{pmatrix} 1 & 0 & 0 & x_0 \\ 0 & 1 & 0 & y_0 \\ 0 & 0 & 1 & z_0 \\ 0 & 0 & 0 & 1 \end{pmatrix} \quad (1)$$

Three Euler angles,  $\alpha$ ,  $\beta$ , and  $\gamma$ , are used to characterize the orientation of the icosahedron, where  $\alpha$  and  $\gamma$  are randomly generated in the interval of  $0-2\pi$  and  $\beta$  is randomly generated in the interval of  $0-\pi$ . A rotational motion of the local coordinate system  $O'-X'Y'Z'$  is then executed to obtain a new coordinate system  $O'-xyz$ , in which the  $z$  axis passes through one of the vertices of the particle, as shown in Figure 2. The rotational matrix  $R$  is expressed as

$$R = \begin{pmatrix} \cos \gamma & -\sin \gamma & 0 \\ \sin \gamma & \cos \gamma & 0 \\ 0 & 0 & 1 \end{pmatrix} \cdot \begin{pmatrix} \cos \beta & 0 & -\sin \beta \\ 0 & 1 & 0 \\ \sin \beta & 0 & \cos \beta \end{pmatrix} \cdot \begin{pmatrix} 1 & 0 & 0 \\ 0 & \cos \alpha & -\sin \alpha \\ 0 & \sin \alpha & \cos \alpha \end{pmatrix} \quad (2)$$

Thus, the geometrical model of the icosahedron in the global coordinate system  $O-XYZ$  can be associated with its vertices  $P_v$  in the new coordinate system  $O'-xyz$ , as expressed by the equation

$$P'_v = RTP_v \quad (3)$$

where  $P'_v$  is the set of vertices of the particle in the global coordinate system  $O-XYZ$  that characterizes the generalized geometrical model of the icosahedron. Similarly, in the global coordinate system  $O-XYZ$ , the generalized geometrical models of the tetrahedron, cube, octahedron, and dodecahedron can also be derived by the same descriptions.

### 3. CONTACT DETECTION ALGORITHM FOR CONVEX POLYHEDRAL PARTICLES

The key issue of random packing of hard particles is to ensure that each hard particle does not overlap with the others. It is therefore essential to detect interparticle contact for a convex polyhedral particle packing model. Unlike spheres or ellipsoids, whose geometrical models can be expressed using simple geometrical functions, convex polyhedral particles do not have overlap potential functions. In other words, it is very difficult to establish a perfect contact theory because the contact should be consistently defined between any two polyhedral particles with various combinations of vertices, edges, and faces in 3D space. Currently, the available contact detection algorithms for convex polyhedra can be categorized as (1) the assembly of simple-shaped particles (e.g., spheres, ellipsoids),<sup>43–45</sup> (2) digital image analysis,<sup>10–15</sup> and (3) numerical algorithms.<sup>46–55</sup> In the method of assembling simple-shaped particles, the profile of a polyhedron is assumed to be composed of a series of simple-shaped particles, and the detection of contact with the simple-shaped particles is used to substitute the detection of contact with the polyhedron.<sup>43–45</sup> However, the accuracy of this method is restricted by the number of particles composing the profile of the polyhedron. As mentioned in section 1, digital image analysis depends on the image resolution of the equipment; for example, the ranges of image resolution by X-ray computed tomography,<sup>10</sup> 3D laser scanner,<sup>11</sup> and atomic force microscopy<sup>15</sup> are 5–50, 100–500, and 0.05–0.1  $\mu\text{m}$ , respectively.

Among numerical algorithms, Cundall<sup>46</sup> introduced the well-known “common plane” (CP) method as early as 1988, which is a plane that, in some sense, bisects the space between the two contacting polyhedral particles. If the two particles are in contact, then both will intersect the CP; otherwise, neither intersects the CP. Consequently, accurately and efficiently searching for the CP between the two particles is crucial. Nezami et al.<sup>47</sup> concluded that the number of iterations searching for the correct CP by Cundall’s method is strongly dependent on the accuracy of the initial guess of the CP. Based on this case, Nezami et al.<sup>47,48</sup> proposed two optimized methods for accurately finding the CP, defined as the fast common plane method (FCPM) and the shortest link method (SLM). Although the two optimized methods dramatically improve the efficiency of searching for the CP compared to the traditional method,<sup>46</sup> the number of iterations for finding the CP by the two methods still cannot be ignored.

On the other hand, some geometrical-model-based numerical algorithms for polyhedral particles have been suggested to judge contact between convex polyhedral particles,<sup>49–55</sup> such as checking vertex-to-vertex, vertex-to-edge, vertex-to-face, edge-to-edge, edge-to-face, and face-to-face contacts in turns. These numerical algorithms can accurately detect contact between polyhedral particles without regard to any iteration steps. Nevertheless, the efficiency of the algorithms is restricted by the number of vertices of the polyhedral particles; in other words, these algorithms have a high computational complexity with a large number of vertices. On the basis of such issues, to avoid iteratively searching for the CP and considering the number of vertices, a numerical algorithm to accurately detect contact between convex polyhedral particles is presented in detail.

Suppose that the computer simulation of random packing of convex polyhedral particles is observed by a finite number of polyhedra. For any two convex polyhedral particles (i.e., Platonic particles  $i$  and  $j$ ), according to eq 3 and Appendix A, the vertices,

edges, and faces of particle  $i$  with its centroid  $\mathbf{C}_i$ , three Euler angles  $(\alpha_i, \beta_i, \gamma_i)$ , the radius  $r_i$  of its circumscribed sphere, and the radius  $R_i$  of its inscribed sphere are given as  $\mathbf{P}'_{vi}$ ,  $\mathbf{S}'_{ei}$ , and  $\mathbf{F}'_{ai}$  respectively. Likewise, the vertices, edges, and faces of particle  $j$  with its centroid  $\mathbf{C}_j$ , the radius  $r_j$  of its circumscribed sphere, and the radius  $R_j$  of its inscribed sphere are written as  $\mathbf{P}'_{vj}$ ,  $\mathbf{S}'_{ej}$ , and  $\mathbf{F}'_{aj}$  respectively. Thus, the algorithm for detecting the contact between particle  $i$  and particle  $j$  can be described as follows:

(1) If the centroidal distance  $d$  between the two particles satisfies the equation

$$d = |\mathbf{C}_i - \mathbf{C}_j| \geq r_i + r_j \quad (4)$$

then no contact occurs.

(2) If the centroidal distance  $d$  between the two particles satisfies the equation

$$d = |\mathbf{C}_i - \mathbf{C}_j| \leq R_i + R_j \quad (5)$$

then contact definitely occurs.

These criteria (i.e., eqs 4 and 5) are just preliminary considerations to improve the efficiency of the initial packing. However, when the distance  $d$  is in the interval between  $r_i + r_j$  and  $R_i + R_j$ , that is,  $R_i + R_j < d < r_i + r_j$ , further effort is needed to determine whether the two particles make contact. Geometrically, two convex polyhedral particles (or convex polygons in 2D space) do not overlap if there is an axis onto which the intervals of projections of the two particles do not intersect (see Figure 3).<sup>56</sup>

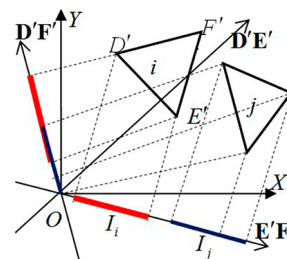


**Figure 3.** Schematic view of the separation axis algorithm (SAA).

This statement is usually referred to as the separation axis algorithm (SAA).

Unlike the CP discussed in the literature, the separation axis does not need to be sought by a series of iteration steps, because it must be one of candidates of the vectors normal to the faces or edges of the 3D polyhedral particles (or the normal vectors of the edges of the 2D polygons), if a separation axis exists. Also, linear transformations (i.e., translation and scaling) of a separation axis do not affect the contact detection of particles.<sup>56</sup> Therefore, it is sufficient to consider the candidates of the normal vectors with unit length that pass through the origin of the global coordinate system, as shown in Figure 3. Figure 3 shows a schematic example for 2D particles, in which  $\mathbf{D}'\mathbf{E}'$ ,  $\mathbf{D}'\mathbf{F}'$ , and  $\mathbf{E}'\mathbf{F}'$  are the unit normal vectors to edges  $D'E'$ ,  $D'F'$ , and  $E'F'$ , respectively, of particle  $i$ . Thus, the intervals  $I_i$  (red segment in Figure 3) and  $I_j$  (blue segment in Figure 3) of projections of the two particles  $i$  and  $j$  onto one of the unit normal vectors can be denoted as in the equations

$$\begin{aligned} I_i &= [\lambda_{\min}^{(i)}(\mathbf{n}), \lambda_{\max}^{(i)}(\mathbf{n})] = [\min\{\mathbf{n} \cdot \mathbf{P}'_{vi}: \mathbf{P}'_{vi} \in \text{particle } i\}, \\ &\quad \max\{\mathbf{n} \cdot \mathbf{P}'_{vi}: \mathbf{P}'_{vi} \in \text{particle } i\}] \end{aligned} \quad (6)$$

$$\begin{aligned} I_j &= [\lambda_{\min}^{(j)}(\mathbf{n}), \lambda_{\max}^{(j)}(\mathbf{n})] = [\min\{\mathbf{n} \cdot \mathbf{P}'_{vj}: \mathbf{P}'_{vj} \in \text{particle } j\}, \\ &\quad \max\{\mathbf{n} \cdot \mathbf{P}'_{vj}: \mathbf{P}'_{vj} \in \text{particle } j\}] \end{aligned} \quad (7)$$

where  $\lambda_{\min}(\mathbf{n})$  and  $\lambda_{\max}(\mathbf{n})$  are the minimum and maximum values, respectively, of projections of vertices  $\mathbf{P}'_v$  of a particle onto the normal vectors  $\mathbf{n}$  (e.g.,  $\mathbf{D}'\mathbf{E}'$ ,  $\mathbf{D}'\mathbf{F}'$ , and  $\mathbf{E}'\mathbf{F}'$ ). If the two intervals  $I_i$  and  $I_j$  do not intersect, that is

$$\lambda_{\min}^{(i)}(\mathbf{n}) > \lambda_{\max}^{(j)}(\mathbf{n}) \quad \text{or} \quad \lambda_{\max}^{(i)}(\mathbf{n}) < \lambda_{\min}^{(j)}(\mathbf{n}) \quad (8)$$

then the two particles  $i$  and  $j$  are definitely nonoverlapping.

Although the implementation of this algorithm is based on 2D convex polygonal particles, the SAA also holds for 3D polyhedral particles. It is worth noting that the vector  $\mathbf{m}$

$$\mathbf{m} = \mathbf{S}'_{ei} \times \mathbf{S}'_{ej} \quad (9)$$

generated by the cross product of two edges, one from each polyhedral particle, needs to be examined for 3D polyhedral particles, if the intervals  $I_i$  and  $I_j$  do not satisfy eq 8.

Analogously, the projected intervals  $J_i$  and  $J_j$  of the two particles  $i$  and  $j$  onto the vector  $\mathbf{m}$  can be written as

$$\begin{aligned} J_i &= [\lambda_{\min}^{(i)}(\mathbf{m}), \lambda_{\max}^{(i)}(\mathbf{m})] = [\min\{\mathbf{m} \cdot \mathbf{P}'_{vi}: \mathbf{P}'_{vi} \in \text{particle } i\}, \\ &\max\{\mathbf{m} \cdot \mathbf{P}'_{vi}: \mathbf{P}'_{vi} \in \text{particle } i\}] \end{aligned} \quad (10)$$

$$\begin{aligned} J_j &= [\lambda_{\min}^{(j)}(\mathbf{m}), \lambda_{\max}^{(j)}(\mathbf{m})] = [\min\{\mathbf{m} \cdot \mathbf{P}'_{vj}: \mathbf{P}'_{vj} \in \text{particle } j\}, \\ &\max\{\mathbf{m} \cdot \mathbf{P}'_{vj}: \mathbf{P}'_{vj} \in \text{particle } j\}] \end{aligned} \quad (11)$$

where  $\lambda_{\min}(\mathbf{m})$  and  $\lambda_{\max}(\mathbf{m})$  are the minimum and maximum projected values, respectively, of vertices  $\mathbf{P}'_v$  of a particle onto the normal vector  $\mathbf{m}$ . If the two intervals  $J_i$  and  $J_j$  satisfy the equation

$$\lambda_{\min}^{(i)}(\mathbf{m}) > \lambda_{\max}^{(j)}(\mathbf{m}) \quad \text{or} \quad \lambda_{\max}^{(i)}(\mathbf{m}) < \lambda_{\min}^{(j)}(\mathbf{m}) \quad (12)$$

then the two convex polyhedral particles  $i$  and  $j$  must be nonoverlapping.

To demonstrate the performance of this algorithm, the accuracy and efficiency of the algorithm were tested. The algorithm was executed on a computer with an Intel E8500 CPU (3.16 GHz) and 4G of RAM. The CPU time (milliseconds) represents the efficiency of the algorithm. Without loss of generality, two pairs of 2D convex polygons were tested to verify the accuracy and efficiency of the present algorithm and compared with the line segment intersection algorithm (SIA) from O'Rourke et al.<sup>57</sup> and Preparata et al.<sup>58</sup> A detailed description of the SIA can be found in ref 58. Parameters and the test results are reported in Table 1. Table 1 includes the test results for the two algorithms with 300 cases. In Table 1,  $i$  and  $j$  represent a pair of convex polygons, the vertices characterize the geometrical information for each polygon, and RP represents the relative position of the pair of polygons reflecting the accuracy of the algorithms. According to the given parameters in Table 1, the two pairs of convex polygons are visualized in Figure 4.

For the two pairs of convex polygons, the relative positions detected by the algorithms are both separated and overlapping as shown in Table 1, in accordance with the results visualized in Figure 4. This suggests the accuracy of the present algorithm, consistent with the reports of O'Rourke et al.<sup>57</sup> and Preparata et al.<sup>58</sup> However, on the basis of the average CPU time, the present algorithm saves more time than the line segment intersection algorithm.<sup>57,58</sup> This indicates that the efficiency of the SAA is superior to that of the SIA.<sup>57,58</sup> The potential reason for the difference could be that the SIA needs to check vertex-to-vertex, vertex-to-edge, and edge-to-edge contacts for

			CPU time (ms)	RP
		vertices		
		Figure 4a		
$i$	$i$	(-29.592, -10.305)	(-40.681, -4.82096)	SAA 14.915
$j$	$j$	(-42.755, -9.9385)	(-45.278, -1.268)	SIA 22.446
		Figure 4b		
$i$	$i$	(25.782, 46.313)	(15.950, 45.366)	SAA 16.351
$j$	$j$	(34.436, 62.454)	(20.506, 47.883)	SIA 27.092
			(18.044, 38.835) (18.96, 47.498)	overlapping
			(25.840, 35.993) (34.552, 41.815)	overlapping
			(27.866, 40.532) (38.603, 50.892)	overlapping

Table 1. Test Comparison between the Separation Axis Algorithm (SAA) and the Segment Intersection Algorithm (SIA)

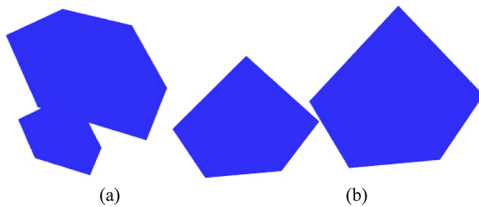


**Figure 4.** Visualizations of convex polygons according to the vertices given in Table 1.

2D convex polygons whereas the SAA needs to detect only whether two intervals of projections of two polygons onto one of the unit normal vectors of the edges satisfy eq 12, if such a separation axis exists; other unit normal vectors of the edges can be ignored. Consequently, according to these test results, the accuracy and efficiency of the present algorithm are favorable.

#### 4. RANDOM SEQUENTIAL PACKING ALGORITHM FOR MONO-/POLYDISPERSE CONVEX POLYHEDRAL PARTICLES

In this section, to simulate the random packing of mono-/polydisperse convex polyhedral particles system with given boundary conditions, a random sequential packing algorithm is introduced as follows:

(1) Input the known parameters, namely, the size of the model container (i.e., the length  $L$ , width  $W$ , and height  $H$  of the prismatic container); the specified size distribution function of polydisperse polyhedra system (which is introduced in the next section), in which the radius  $r_i$  of the circumscribed sphere of polyhedron is used to stand for its size; the total volume fraction  $V_{\text{agg}}$  of particles, which is used to determine the total number  $N$  of mono-/polydisperse particles.

(2) Define the boundary conditions of the container. If rigid boundary conditions are used, particles are not allowed to traverse through rigid boundary planes of the container; if periodic boundary conditions are used, particles can intersect with the periodic boundary planes, and a so-called periodic compensation technology should be implemented. Xu et al.<sup>59</sup> described the details of periodic compensation technology.

(3) For a polydisperse particle packing system, the sizes  $r_i$  of polydisperse polyhedral particles should be arranged in descending order, where  $i = 1, 2, \dots, N$ .

(4) Randomly generate the centroid  $\mathbf{C}_i$  of particle  $i$  in the model structure, where  $i = 1, 2, \dots, N$ .

(5) Randomly generate three Euler angles  $\alpha_i$ ,  $\gamma_i$  and  $\beta_i$  of the particle  $i$  in the intervals  $[0, 2\pi]$  and  $[0, \pi]$ , where  $i = 1, 2, \dots, N$ .

(6) Calculate the geometrical model including the vertices  $\mathbf{P}'_{vi}$ , edges  $S'_{vi}$ , and faces  $F'_{ai}$  of particle  $i$  according to eq 3 and Appendix A, where  $i = 1, 2, \dots, N$ .

(7) Judge whether generated particle  $i$  intersects with the rigid boundary planes. If it does, return to steps 4 and 5 to regenerate particle  $i$ . Judge whether generated particle  $i$  intersects with the periodic boundary planes. If it does, (virtually) replicate particle  $i$  at the corresponding locations by virtue of periodic compensation technology.<sup>59</sup>

(8) Detect whether generated particle  $i$  and its duplicate particles (if any) overlap with all preceding  $i - 1$  particles; if it does, return to steps 4 and 5 to regenerate particle  $i$ . Otherwise, return to steps 4 and 5 to generate particle  $i + 1$ .

(9) Iterate steps 4–8 until all  $N$  particles have been generated.

In this algorithm, the key issues are identifying intersections between a particle and a container wall (i.e., a plane) and identifying interparticle contact (as presented in section 3). The geometrical algorithm used to check the intersection between a convex polyhedral particle and a plane is elaborated next.

As an introductory example, consider the problem of detecting the intersection between an octahedron  $O_c$  with centroid  $\mathbf{C}_o$ , three Euler angles  $(\alpha_o, \beta_o, \gamma_o)$ , radius  $r_o$  of its circumscribed sphere, and radius  $R_o$  of its inscribed sphere, and a spatial plane expressed by

$$\mathbf{N} \cdot (\mathbf{P} - \mathbf{P}_0) = 0 \quad (13)$$

where  $\mathbf{N}$  is a vector normal to the plane and  $\mathbf{P}$  and  $\mathbf{P}_0$  are an arbitrary point and a fixed point, respectively, on the plane. The geometrical algorithm is presented next.

First, a preliminary judgment is implemented by calculating the distance  $d_c$  from the centroid of the particle to the plane, according to the equation

$$d_c = \frac{|\mathbf{N} \cdot (\mathbf{C}_o - \mathbf{P}_0)|}{\|\mathbf{N}\|} \quad (14)$$

where  $\|\cdot\|$  represents the norm of a vector. For  $d_c \leq R_o$ , intersection definitely occurs; for  $d_c \geq r_o$ , no intersection occurs. Otherwise, the faces comprising the octahedron need to be further observed.

Second, suppose that one triangular face  $F_{a1}$  of the octahedron consists of three vertices  $\mathbf{P}'_{v1}, \mathbf{P}'_{v2}$ , and  $\mathbf{P}'_{v3}$ . To determine whether the plane and  $F_{a1}$  intersect, the signed distances  $\mathbf{d}_1, \mathbf{d}_2$ , and  $\mathbf{d}_3$  from the three vertices  $\mathbf{P}'_{v1}, \mathbf{P}'_{v2}$ , and  $\mathbf{P}'_{v3}$  to the plane should be computed as

$$\mathbf{d} = \frac{\mathbf{N} \cdot (\mathbf{P}'_{v1} - \mathbf{P}_0)}{\pm \|\mathbf{N}\|} \quad (\mathbf{P}'_v = \mathbf{P}'_{v1}, \mathbf{P}'_{v2}, \text{ or } \mathbf{P}'_{v3}) \quad (15)$$

where  $\pm$  depends on the dot product of  $\mathbf{N}$  and  $\mathbf{P}_0$ . Then, their signs are compared as follows:

(1) If all of the vertices of  $F_{a1}$  are on the side of the plane, as shown in Figure 5a, the three signed distances satisfy the relations

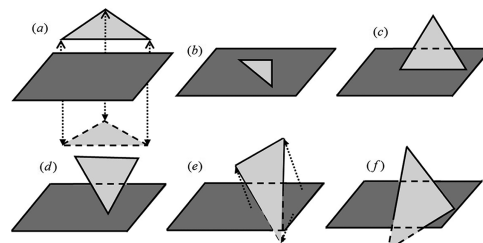


**Figure 5.** Relationships of the spacing positions between the plane and the triangular face.

$\mathbf{d}_1 > 0, \mathbf{d}_2 > 0$ , and  $\mathbf{d}_3 > 0$  or  $\mathbf{d}_1 < 0, \mathbf{d}_2 < 0$ , and  $\mathbf{d}_3 < 0$ , in which case the plane and  $F_{a1}$  do not certainly intersect.

(2) If  $F_{a1}$  and the plane are coplanar, in other words,  $\mathbf{d}_1 = 0, \mathbf{d}_2 = 0$ , and  $\mathbf{d}_3 = 0$ , then the plane and  $F_{a1}$  are not considered as an intersection, as shown in Figure 5b.

(3) If two vertices of  $F_{a1}$  are located on the plane, as shown in Figure 5c, then the three signed distances satisfy  $\mathbf{d}_1 = 0$  and  $\mathbf{d}_2 = 0, \mathbf{d}_3 = 0$  and  $\mathbf{d}_3 = 0$ , or  $\mathbf{d}_2 = 0$  and  $\mathbf{d}_3 = 0$ . In this case, no intersection exists.

(4) If one vertex of  $F_{a1}$  is located on the plane and the other two vertices are on one side of the plane, as depicted in Figure 5d, then  $\mathbf{d}_1 = 0, \mathbf{d}_2 > 0$ , and  $\mathbf{d}_3 > 0$ ;  $\mathbf{d}_1 = 0, \mathbf{d}_2 < 0$ , and  $\mathbf{d}_3 < 0$ ; or  $\mathbf{d}_2 = 0$ ,

$d_1 > 0$ , and  $d_3 > 0$ ;  $d_2 = 0$ ,  $d_1 < 0$ , and  $d_3 < 0$ ;  $d_3 = 0$ ,  $d_1 > 0$ , and  $d_2 > 0$ ; or  $d_3 = 0$ ,  $d_1 < 0$  and  $d_2 < 0$ . In this case, no intersection occurs.

(5) If one of the vertices of  $F_{a1}$  is on the opposite side of the plane as the other two, as depicted in Figure 5e, then  $d_1 > 0$ ,  $d_2 < 0$ , and  $d_3 < 0$ ;  $d_1 < 0$ ,  $d_2 > 0$ , and  $d_3 > 0$ ;  $d_2 > 0$ ,  $d_1 < 0$ , and  $d_3 < 0$ ;  $d_2 < 0$ ,  $d_1 > 0$ , and  $d_3 > 0$ ;  $d_3 > 0$ ,  $d_1 < 0$ , and  $d_2 < 0$ ; or  $d_3 < 0$ ,  $d_2 > 0$ , and  $d_1 > 0$ . In this case, the plane and  $F_{a1}$  definitely intersect.

(6) If one vertex of  $F_{a1}$  is located on the plane and the other two vertices are on the opposite side of the plane, as shown in Figure 5f, then  $d_1 = 0$ ,  $d_2 > 0$ , and  $d_3 < 0$ ;  $d_1 = 0$ ,  $d_2 < 0$ , and  $d_3 > 0$ ;  $d_2 = 0$ ,  $d_1 > 0$ , and  $d_3 < 0$ ;  $d_2 = 0$ ,  $d_1 < 0$ , and  $d_3 > 0$ ;  $d_3 = 0$ ,  $d_1 > 0$ , and  $d_2 < 0$ ; or  $d_3 = 0$ ,  $d_1 < 0$ , and  $d_2 > 0$ . In this case, intersection certainly exists.

In terms of this geometrical algorithm, as long as a single face of the polyhedron intersects the boundary plane of the container, the particle is regarded as intersecting with the container. If all of the faces of the polyhedron do not intersect with the boundary plane, no intersection occurs between the particle and the boundary plane of the container.

## 5. APPLICATION

As particulate composite materials, cementitious materials can be considered as three-phase composite structures at the microscopic scale, composed of aggregate particles, cement paste, and a relatively porous interfacial transition zone (ITZ).<sup>1,2,64,70</sup> (It has been experimentally and numerically validated that ITZ exists around aggregate particles in cementitious materials.<sup>63,65,70</sup>) In the three-phase composite microstructure, hard aggregate particles are randomly dispersed in the matrix of cement paste, and each hard aggregate particle is coated with a soft shell with a constant thickness, which is represented by the ITZ. This is known as the hard core/soft shell model.<sup>2,77,78</sup> ITZ microstructure characteristics such as the ITZ thickness and ITZ volume fraction play an important role in the macroscopic physical properties of cementitious materials. Such microstructure characteristics are, in turn, dependent on the mesostructure information of cementitious materials, such as the volume fraction  $V_V$ , the specific surface area  $S_V$ , and the mean free spacing  $\lambda$  of the solid phase.

For instance, the ITZ thickness is normally reflected by the distance corresponding to the stable value of the curve of the volume fraction  $V_V$  of the solid phase from the boundary layers to the center of the mesostructure model.<sup>68,69</sup> In addition, the specific surface area  $S_V$  of the solid phase and the ITZ thickness also influence the ITZ volume fraction. Recently, Xu and Chen<sup>2</sup> developed an analytical formula for the volume fraction of the ITZ around ellipsoidal aggregate particles, given by

$$V_{ITZ} = (1 - V_{agg}) \left( 1 - \exp \left\{ -\frac{S_V}{1 - V_{agg}} \right. \right. \\ \times \left[ t + \left( \frac{2\pi \langle D_{eq} \rangle}{\langle S \rangle} + \frac{S_V}{2(1 - V_{agg})} \right) t^2 + \frac{2\pi}{3\langle S \rangle} \left( 2 + \frac{S_V \langle D_{eq} \rangle}{1 - V_{agg}} \right) t^3 \right] \left. \right) \quad (16)$$

where  $V_{ITZ}$ ,  $t$ , and  $S_V$  are the ITZ volume fraction, ITZ thickness, and specific surface area of the solid phase, respectively. Detailed descriptions can be found in our recent work.<sup>2</sup> It can be seen from eq 16 that the ITZ volume fraction depends strongly on the specific surface area  $S_V$  of the solid phase and the ITZ thickness  $t$ . Furthermore, on the basis of the classical composite material

theory, many different kinds of multiphase composite models have been developed to consider the effects of the microstructure of the ITZ on the effective physical properties (e.g., thermal/electrical conductivity, ion diffusivity, dielectric constant, and elastic modulus) of cementitious materials, such as the single/multilayer composite sphere model,<sup>64</sup> the generalized self-consistent model,<sup>6</sup> and the differential effective medium model.<sup>77</sup> In these models, the most important parameter is the volume fraction of each phase. Once the volume fraction of the ITZ is determined, the effective physical properties of such the three-phase composite structure can be computed by such classical composite models. On the other hand, the mean free spacing  $\lambda$  is the average of all unobstructed surface-to-surface distances to neighboring particles;<sup>67</sup> its third power is usually considered to be inversely proportional to the global bond strength of cementitious materials (i.e.,  $F = A/\lambda^{-3}$ , where  $F$  and  $A$  are the global bond strength and van der Waals constant, respectively),<sup>61,68–71</sup> as physical interparticle bonding forces should contribute to the “strength” of particulate materials such as cementitious materials.

From the mesoscale point of view, cementitious materials can be considered as two-phase composite materials, composed of hard aggregate particles and cement paste. The random packing behaviors of these aggregate particles directly affect the mesostructure characteristics of cementitious materials, such as the volume fraction  $V_V$ , the specific surface area  $S_V$ , and the mean free spacing  $\lambda$  of the solid phase. Moreover, such mesostructure information is crucial in investigating the microstructure characteristics of the ITZ and the macroscopic physical properties of cementitious materials. However, in the modeling of the mesostructure of cementitious materials, most works have focused on the packing of systems of spherical or ellipsoidal particles.<sup>2,4,16–18,61–65</sup> The influence of polyhedral-shaped particles on the mesostructure has been minimally considered in the literature.

Based on the algorithms presented thus far, the random packing models of monodisperse Platonic particles were first simulated to investigate the effect of particle shape on the packing structure. Then, the packing structures of polydisperse Platonic particles with a specified size distribution function were established to represent the mesostructure models of cementitious materials. Also, all of the packing structures of the mono-/polydisperse particles were quantitatively evaluated by employing stereological theory and a sectioning analysis method.

**5.1. Mesostructure Models of Monodisperse Platonic Particles.** To investigate the effects of particle shape on the particle packing structure, the random packing models of monodisperse particles with various shapes, including cubic, octahedral, dodecahedral, icosahedral, oblate ellipsoidal (i.e., the aspect ratio of  $\kappa = 0.7$ ), prolate ellipsoidal (i.e., the aspect ratio of  $\kappa = 2.5$ ), and spherical, were simulated first. It is noted that tetrahedral particles were not considered in this work, because their shape is too sharp to represent the shape of practical aggregate particles in cementitious materials. Applying the algorithms described in the preceding sections, including the interparticle contact detection algorithm, the particle-to-container wall intersection detection algorithm, and the random sequential packing algorithm, the random packing models of the four types of monodisperse Platonic particles were constructed. In addition, the random packing models of ellipsoidal and spherical particles were presented in our preliminary works.<sup>16–18</sup> Thus, Figure 6 shows the random packing models of monodisperse particles with these shapes. In these models, the initial parameters were set as a volume

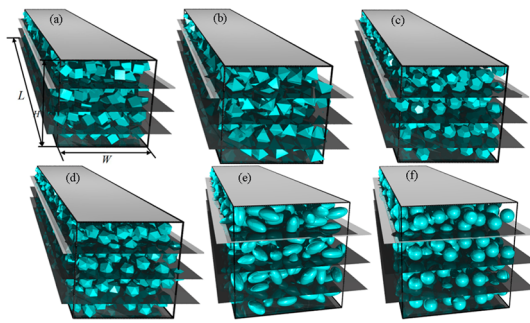


**Figure 6.** Schematic views of random packing models of monodisperse particles with (a) cubic, (b) octahedral, (c) dodecahedral, (d) icosahedral, (e) prolate ellipsoidal (aspect ratio of  $\kappa = 2.5$ ), and (f) spherical shapes.

fraction of particles of  $V_{\text{agg}} = 0.3$ , an equivalent diameter (its definition can be found in section 5.3) of particles of  $D_{\text{eq}} = 10 \text{ mm}$ , and a prismatic container with a length of  $L = 800 \text{ mm}$  and a width and height of  $W = H = 200 \text{ mm}$ . Herein, semiperiodic boundary conditions were assigned to the model structure so as to consider the influence of wall effects on particle packing along the rigid surface. Specifically, the top and low long planes were set as rigid boundary conditions, and the other four planes were set as periodic boundary conditions, as depicted in Figure 6.

To validate the reliability of the mesostructure models and the algorithms developed in this work, the sectioning morphology characteristics of the Platonic particle packing structures from an arbitrary sectioning plane were displayed by sectioning analysis methods. In addition, such sectioning morphology information is of significance for analyzing and understanding convex polyhedral particle packing structures (as introduced later). Nevertheless, convex polyhedral particles, unlike spherical or ellipsoidal particles, are not associated with mathematical functions that allow direct access to sectioning morphology characteristics. Currently, little is known about how to obtain sectioning morphology characteristics of convex polyhedral particle packing structures. In this work, a sectioning analysis algorithm is presented to derive such sectioning morphologies. Actually, it is certain that the sectioning morphology of a convex polyhedron must be a convex polygon, because the cross section is regarded as nonexistent when the convex polyhedron and the sectioning plane intersect at a line segment or a point. Based on this case, the sectioning analysis algorithm is described as follows:

(1) Input the equation of a sectioning plane, as given in eq 13.

(2) Judge whether polyhedral particle  $i$  in the model structure intersects the sectioning plane. (The intersection detection between a convex polyhedral particle and a plane was demonstrated in section 4.) If no intersection exists, observe particle  $i + 1$ . Otherwise, derive a collection of intersection points of each face of the polyhedron intersecting the sectioning plane, by computing the signed distance from each vertex of all the faces and comparing the signs.<sup>56,60</sup> Note that, during data collection, there might be some repetitive points because each vertex must be shared by at least one face.

(3) Delete the repetitive points within the collection of intersection points. The remainder is the set of valid points comprising the convex polygon (i.e., sectioning morphology). However, it is undesirable that the connections of these valid points might consist of a concave polygon. Therefore, to reflect a realistic sectioning morphology, it is necessary to rearrange these points in a reasonable order so that they can be composed into a correct convex polygon.

(4) The basic principle of sorting these points is to ensure that the connection of neighboring points constitutes one edge of the realistic convex polygon; in other words, the other points should be on the side of the connection of the neighboring points. Thus, the details of the sort should be implemented as follows:

(4a) Select one arbitrary point (e.g.,  $p_0$ , as shown in Figure 7) as an initial point in the collection.

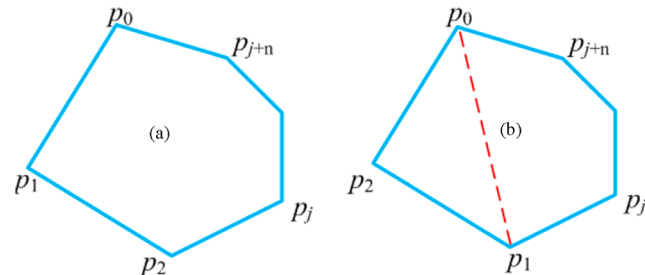


**Figure 7.** Schematic view of the types of valid points composing a convex polygon.

(4b) Check whether the connection of the initial point  $p_0$  with its adjacent point (i.e.,  $p_1$ ) constitutes one edge of the convex polygon.

(4c) If the points other than  $p_0$  and its adjacent point are on the side of the connection, as shown in Figure 7a, the connection of  $p_0$  with  $p_1$  must be one edge of the convex polygon. The initial point  $p_0$  is then deposited in a new object  $E$ , and  $p_1$  is considered as a new initial point  $p_0$  to judge the next adjacent point by step 4b.

(4d) If one point is on the opposite side of the connection line between  $p_0$  and  $p_1$  than the other points, as shown in Figure 7b, the connection of  $p_0$  with  $p_1$  is not a correct edge of the convex polygon. Then,  $p_0$  is kept constant, and the connection of  $p_0$  with the next point (i.e.,  $p_2$ ) need to be further examined according to step 4b until the connection of  $p_0$  with a certain point constitutes one edge of the convex polygon.

(5) Finally, an accurate convex polygon can be constructed by connecting in turn those points deposited in object  $E$ . Moreover, based on these points, the area  $A$  and perimeter  $C$  of the convex polygon can be determined<sup>66</sup> as

$$A = \frac{1}{2} \sum_{i=1}^n (x_i y_{i+1} - x_{i+1} y_i) \quad (17)$$

$$C = \sum_{i=1}^n \sqrt{(x_{i+1} - x_i)^2 + (y_{i+1} - y_i)^2} \quad (18)$$

where  $n$  is the number of points comprising the convex polygon and  $(x_i, y_i)$  and  $(x_{i+1}, y_{i+1})$  are the coordinates of points  $i$  and  $i + 1$ , respectively. To close the polygon, the first and last vertices are the same, namely,  $x_1, y_1 = x_n, y_n$ .

According to the sectioning analysis algorithm, a series of sectioning planes (i.e., gray planes shown in Figure 6) paralleling the rigid boundary walls were applied to intercept the four Platonic particles packing structures. Figure 8 presents the four sectioning morphology characteristics corresponding to the four packing models. It can be seen from Figure 8 that these sectioning morphologies are convex polygons, and no overlapping appears among the polygons. Moreover, the periodic compensation mechanism is also reflected in the 2D sectioning planes. Therefore, these results demonstrate that the reliability of the algorithms presented in this work and the random packing structures of the monodisperse Platonic particles are favorable.

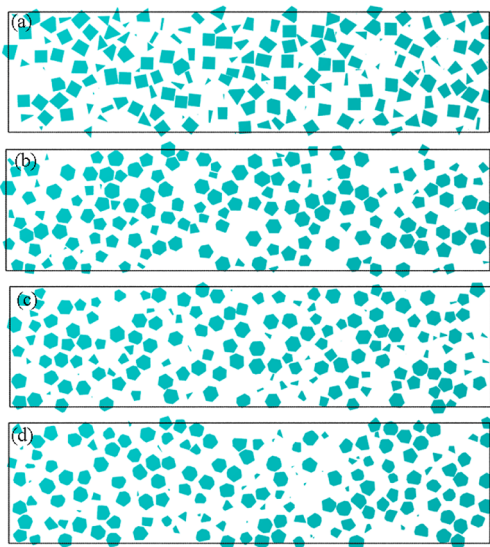


**Figure 8.** Sectioning morphologies corresponding to the four Platonic particles packing structures in Figure 6.

**5.2. Quantitative Evaluation of Monodisperse Particle Packing Models.** In this section, on the basis of the sectioning morphology analysis algorithm developed in the preceding section, a research strategy is proposed to quantitatively characterize the mesostructure models composed of monodisperse particles, namely, the quantitative stereology and serial sectioning analysis technique. Stereology combines geometry and probability theories and is therefore also referred to as geometric probability theory. It allows “extrapolation” from data collected in 2D sectioning characteristics to 3D reality.<sup>67</sup> In other words, the 3D configuration parameters of the mesostructure, such as the volume fraction  $V_V$ , specific surface area  $S_V$ , and mean free spacing between particles  $\lambda$ , can be estimated in an unbiased manner from 2D observations.

Based on the quantitative stereology, the area fraction  $A_A$  of the solid phase is an unbiased estimator of the volume fraction  $V_V$  of the solid phase (i.e.,  $A_A = V_V$ ). The perimeter length of the solid features per unit test area  $L_A$  allows for the estimation of the specific surface area  $S_V$  of the solid phase (i.e.,  $L_A = \pi S_V / 4$ ). Also, the mean free spacing between particles  $\lambda$  is calculated according to the equation

$$\lambda = \frac{\pi(1 - A_A)}{L_A} = \frac{4(1 - V_V)}{S_V} \quad (19)$$

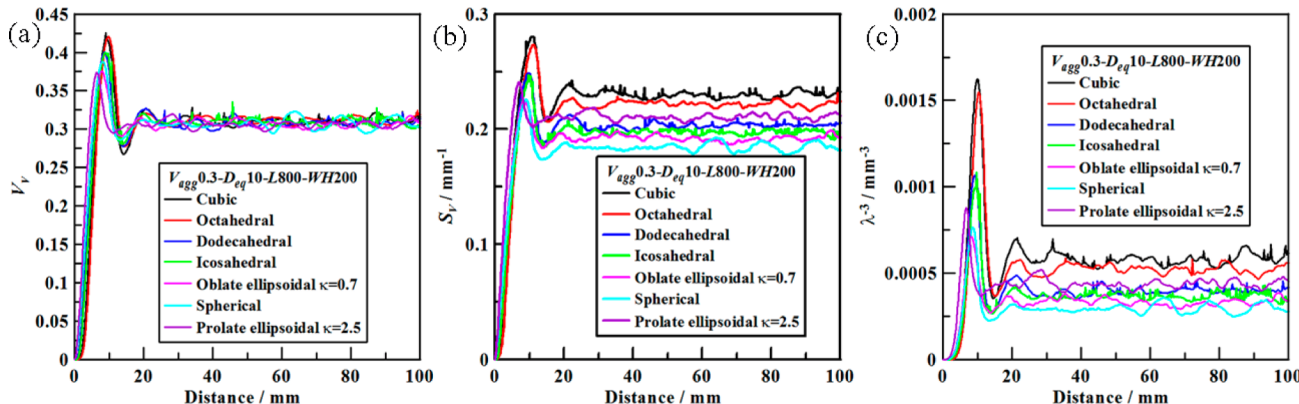


**Figure 9.** Quantitative characterization of the configuration parameters of the monodisperse particle packing system: (a)  $V_V$ , (b)  $S_V$ , and (c)  $\lambda^{-3}$  versus distance.

Therefore, these configuration parameters were combined with the sectioning analysis technique to quantitatively investigate the mesostructure of solid phase.

With the mesostructure models of monodisperse particles with various shapes simulated in the preceding section, the effect of the particle shape on the monodisperse particle packing structure was investigated quantitatively. The initial parameter set for each model structure was the same as in the preceding section (section 5.1). Figure 9 presents the simulated results for  $V_V$ ,  $S_V$ , and  $\lambda^{-3}$  versus distance from the rigid boundary plane to the center of a single model structure with different particle shapes [i.e., cubic, octahedral, dodecahedral, icosahedral, oblate ellipsoidal ( $\kappa = 0.7$ ), prolate ellipsoidal ( $\kappa = 2.5$ ), and spherical].

For the same initial parameters, Figure 9 shows that the characteristics of the three configuration parameters  $V_V$ ,  $S_V$ , and  $\lambda^{-3}$  for different particle shapes are similar from the rigid boundary wall to the central region; specifically, they first increase dramatically, then decrease, increase again, and ultimately fluctuate slightly around a specific value. Herein, the specific value of each model structure is considered as the average value of the model structure. Thus, from Figure 9a, the average values of  $V_V$  for different particle shapes are approximately consistent and equal to the given volume fraction ( $V_{agg} = 0.3$ ) of particles. This indicates that the effect of particle shape on the configuration parameter  $V_V$  is weak. However, the average values of  $S_V$  and  $\lambda^{-3}$  for different particle shapes are not in agreement. Figure 9b,c presents the average values of  $S_V$  and  $\lambda^{-3}$  in the order cubic particles > octahedral particles > prolate ( $\kappa = 2.5$ ) ellipsoidal particles > dodecahedral particles > icosahedral particles > oblate ( $\kappa = 0.7$ ) ellipsoidal particles > spherical particles. In other words, the global bond strengths of cementitious materials composed of monodisperse particles are also in the order cubic particles > octahedral particles > prolate ( $\kappa = 2.5$ ) ellipsoidal particles > dodecahedral particles > icosahedral particles > oblate ( $\kappa = 0.7$ ) ellipsoidal particles > spherical particles.

To quantitatively evaluate the influence of particle shape on the two configuration parameters  $S_V$  and  $\lambda^{-3}$ , these particle shapes first need to be unified by a shape parameter. For an ellipsoidal particle, it is convenient to use the aspect ratio ( $\kappa$ ) as the shape parameter. For a polyhedral particle, however, it is not necessarily clear how to unify polyhedral particle shapes with those of ellipsoidal particles. Fortunately, Brown<sup>72</sup> and Zhou et al.<sup>73,74</sup> introduced sphericity, which is defined as the ratio of the surface area between a sphere and a nonspherical particle

with the same volume, to reflect the shape of nonspherical particles. Here, sphericity is used to unify these particle shapes, and the values of sphericity for particles with different shapes are listed in Table 2. From Figure 9b,c and Table 2, it can be seen that

**Table 2. Comparison of the Theoretical and Simulated Results for  $S_V$  and  $\lambda^{-3}$  for the Random Packing of Monodisperse Particles with Different  $s$  Values**

		$(S_V, \lambda^{-3})$	
$s$		simulated results	theoretical results
0.806	cube	$(0.23 \pm 7 \times 10^{-3}, 0.0006 \pm 6 \times 10^{-5})$	$(0.223, 0.00051)$
0.845	octahedron	$(0.22 \pm 5 \times 10^{-3}, 0.0005 \pm 5 \times 10^{-5})$	$(0.213, 0.00044)$
0.885	$\kappa = 2.5$	$(0.21 \pm 5 \times 10^{-3}, 0.0004 \pm 5 \times 10^{-5})$	$(0.203, 0.00038)$
0.910	dodecahedron	$(0.20 \pm 6 \times 10^{-3}, 0.0004 \pm 2 \times 10^{-5})$	$(0.198, 0.00035)$
0.939	icosahedron	$(0.20 \pm 3 \times 10^{-3}, 0.0003 \pm 8 \times 10^{-5})$	$(0.192, 0.00032)$
0.977	$\kappa = 0.7$	$(0.19 \pm 4 \times 10^{-3}, 0.0003 \pm 3 \times 10^{-5})$	$(0.184, 0.00028)$
1	sphere	$(0.18 \pm 7 \times 10^{-3}, 0.0002 \pm 9 \times 10^{-5})$	$(0.180, 0.00026)$

the simulated results for  $S_V$  and  $\lambda^{-3}$  decrease with increasing sphericity. Subsequently, to verify the reliability of the results for  $S_V$  and  $\lambda^{-3}$  simulated by the present methodology, the theoretical results for  $S_V$  and  $\lambda^{-3}$  for random packing structures of monodisperse nonspherical particles with different particle shapes were derived. According to stereological theory,<sup>67</sup>  $S_V$  can be written as

$$S_V = \frac{V_{\text{agg}} S(D_{\text{eq}})}{V(D_{\text{eq}})} \quad (20)$$

where  $V(D_{\text{eq}})$  and  $S(D_{\text{eq}})$  are the volume and surface area, respectively, of a single particle with diameter  $D_{\text{eq}}$  that is

$$V(D_{\text{eq}}) = \frac{\pi}{6} D_{\text{eq}}^3 \quad (21)$$

$$S(D_{\text{eq}}) = \frac{\pi D_{\text{eq}}^2}{s} \quad (22)$$

where  $s$  is the sphericity of the single particle with diameter  $D_{\text{eq}}$ . For monodisperse particle packing systems, the equivalent diameter  $D_{\text{eq}}$  represented as a nonspherical particle size (as introduced in the next section) is constant.

Thus, upon substituting eqs 21 and 22 into eq 20, the theoretical results for  $S_V$  and  $\lambda^{-3}$  for monodisperse nonspherical particle packing structures are given by

$$S_V = \frac{6V_{\text{agg}}}{sD_{\text{eq}}} \quad (23)$$

$$\lambda^{-3} = \left[ \frac{4(1 - V_V)}{S_V} \right]^{-3} = \left[ \frac{2sD_{\text{eq}}(1 - V_{\text{agg}})}{3V_{\text{agg}}} \right]^{-3} \quad (24)$$

The theoretical results for  $S_V$  and  $\lambda^{-3}$  with different  $s$  values obtained by substituting the initial parameters into eqs 23 and 24, such as  $D_{\text{eq}} = 10$  mm and  $V_{\text{agg}} = 0.3$ , are reported in Table 2. From Table 2, it can be seen that the theoretical results for  $S_V$  and  $\lambda^{-3}$  decrease with increasing  $s$ , which is consistent with the simulated

results. Furthermore, the theoretical values for  $S_V$  and  $\lambda^{-3}$  present good agreement with the average values for the monodisperse particle packing structures. Consequently, the reliability of the simulated results for  $S_V$  and  $\lambda^{-3}$  for the random packing structures of monodisperse nonspherical particles with different shapes is good.

**5.3. Mesostructure Model of Polydisperse Platonic Particles.** In practical cementitious materials, the size of particles is not monodisperse, but polydisperse. In other words, the size of particles satisfies a specific size distribution in cementitious materials.<sup>9,70</sup> Normally, the particle size distribution (PSD) can be obtained by a conventional sieve analysis test or laser particle analysis. However, in computer simulations, polyhedral particle size distributions (PPSDs) are seldom reported. In this work, an equivalent diameter  $D_{\text{eq}}$ <sup>17,18,68</sup> which is defined as the diameter of a sphere having the same volume as the Platonic particle, is introduced to define the PPSD. Additionally, the relationship between the equivalent diameter  $D_{\text{eq}}$  and the size  $r$  (i.e., the radius of the circumscribed sphere) of each Platonic particle is presented in Appendix B. Thus, the size parameter  $r$  of each Platonic particle can be substituted by its equivalent diameter  $D_{\text{eq}}$ . This means that the equivalent spherical particle size distribution can be related to the PPSD.

In cementitious materials, the PSD of spheroidal aggregates, which stands for the lower bound of aggregates,<sup>17,69</sup> is commonly represented by the Fuller distribution function

$$f_N(D) = \frac{2.5D_{\text{max}}^{2.5}D_{\text{min}}^{2.5}}{(D_{\text{max}}^{2.5} - D_{\text{min}}^{2.5})D^{3.5}} \quad (25)$$

where  $f_N(D)$  is the number-based probability density function of spheroidal aggregates;  $D$  is the diameter of a spheroidal aggregate (mm); and  $D_{\text{max}}$  and  $D_{\text{min}}$  are the maximum and minimum diameters (mm), respectively. Replacing  $D$  in eq 25 with  $D_{\text{eq}}$ , the PPSD can be expressed as

$$f_N(D_{\text{eq}}) = \frac{2.5D_{\text{max eq}}^{2.5}D_{\text{min eq}}^{2.5}}{(D_{\text{max eq}}^{2.5} - D_{\text{min eq}}^{2.5})D_{\text{eq}}^{3.5}} \quad (26)$$

where  $D_{\text{max eq}}$  and  $D_{\text{min eq}}$  are the maximum and minimum equivalent diameters (mm), respectively, of the polyhedral particle.

Thus, according to the modified Fuller distribution function (see eq 26), the particle number of polyhedral aggregates with various sizes can be obtained with a given volume fraction  $V_{\text{agg}}$  of aggregates; detailed descriptions of the PSD have been found in previous research.<sup>69</sup> With the particle number of polydisperse polyhedral aggregates with various sizes and the algorithms presented in sections 3 and 4, a mesostructure model of cementitious materials with semiperiodic boundary conditions can be constructed. As an example, Figure 10 visualizes four mesostructure models composed of the random packings of polydisperse cubic, octahedral, dodecahedral, and icosahedral particles. In these model structures, the initial parameters are set as  $D_{\text{max eq}} = 45$  mm,  $D_{\text{min eq}} = 5$  mm, and  $V_{\text{agg}} = 0.42$ , and the size and boundary conditions of the model structures are consistent with those of the monodisperse particle model structures.

Furthermore, by virtue of the sectioning analysis algorithm developed in section 5.1, the sectioning morphology characteristics of the polydisperse particle packing structures were derived to validate the reliability of the mesostructure models. Figure 11

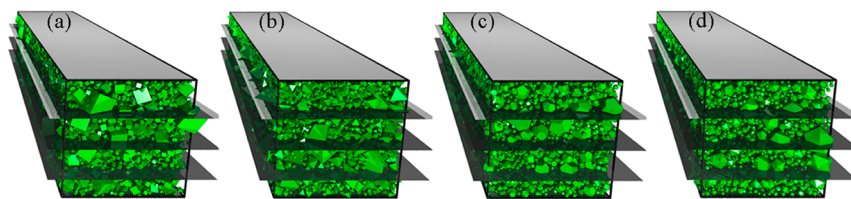


**Figure 10.** Mesostructure models composed of random packings of polydisperse (a) cubic, (b) octahedral, (c) dodecahedral, and (d) icosahedral particles.

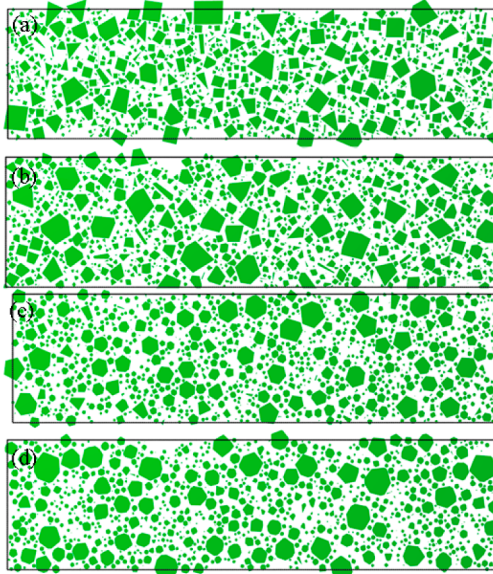


**Figure 11.** Sectioning morphologies corresponding to the four polydisperse Platonic particles packing structures shown in Figure 10.

depicts four sectioning morphology characteristics corresponding to the four mesostructure models. It can be seen from Figure 11 that these sectioning morphologies are convex polygons with no overlapping among the polygons. Therefore, these results suggest that the reliability of the mesostructure models is favorable.

**5.4. Quantitative Characterization of Polydisperse Particle Packing Models.** With the mesostructure models of polydisperse particles simulated in the preceding section, the dependence of such mesostructure models on particle shape,

such as cubic, octahedral, dodecahedral, and icosahedral, was quantitatively investigated by the sectioning morphology analysis algorithm and quantitative stereology (illustrated in section 5.2). The initial parameter set of each model structure was the same as in section 5.3. To guarantee the reliability of the simulated results, 200 model structures were generated for each particle shape. Figure 12 presents the statistical results for  $V_V$ ,  $S_V$ , and  $\lambda^{-3}$  versus distance from the rigid boundary plane to the center of the model structure. Furthermore, the statistical results were compared with those for ellipsoidal particles [including oblate ellipsoids ( $\kappa = 0.7$ ), spheres ( $\kappa = 1$ ), and prolate ellipsoids ( $\kappa = 2.5$ )] developed in our previous work,<sup>69</sup> as shown in Figure 12.

It can be seen from Figure 12a that the curves of  $V_V$  for the different polydisperse particle packing structures were basically uniform, consisting of an ascending part and a plateau, in agreement with the results for ellipsoidal particles<sup>17,18,69</sup> but different from the results for the monodisperse particle packing structures. Moreover, the stable volume fraction ( $V_V = 0.43 \pm 0.007$ ) of the solid phase representing the average value of  $V_V$  for the packing structures was slightly higher than the given volume fraction ( $V_{agg} = 0.42$ ) of the aggregates. The reason for this discrepancy is that, in the computer simulations, the ratio of the maximum particle size ( $D_{max eq}$ ) to the height ( $H$ ) of the prismatic container was 0.225, so that the wall effects of the prismatic model structure cannot be completely neglected.<sup>69,75</sup> However, these results reveal that the effect of particle shape on the configuration parameter  $V_V$  is negligible, irrespective of the mono-/polydisperse particle packing structure.

To validate the reliability of the results for  $V_V$  simulated using the present methodology, the experimental results from Yang and Yan<sup>76</sup> were compared with the simulated results. In the experiments of Yang and Yan,<sup>76</sup> the aggregate size ranges were set as 5–25 and 5–31.5 mm, the volume fraction of aggregates

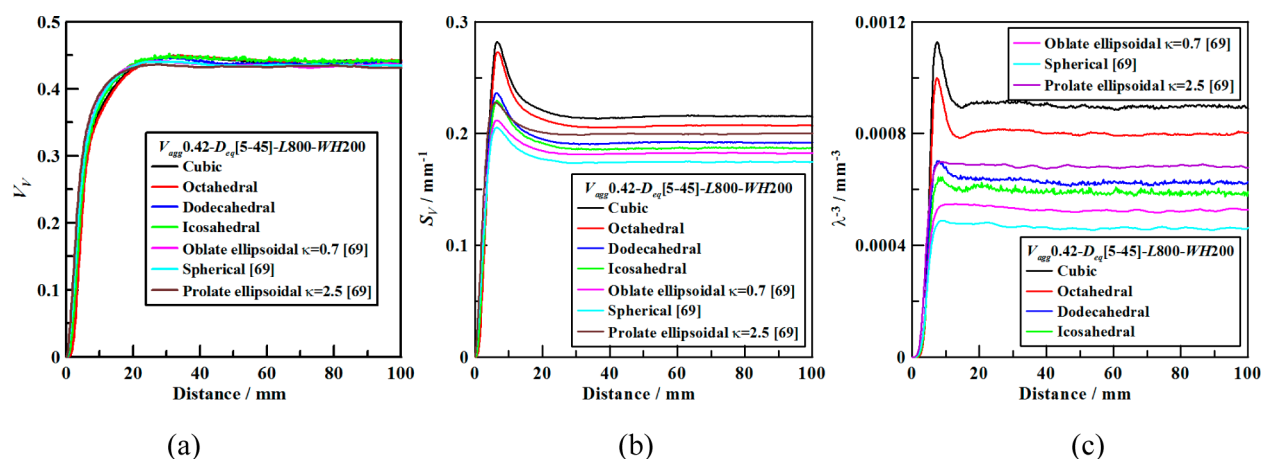


**Figure 12.** Quantitative characterization of the configuration parameters of the polydisperse particle packing system: (a)  $V_V$ , (b)  $S_V$ , and (c)  $\lambda^{-3}$  versus distance.

in concrete was  $V_{\text{agg}} = 0.50$ , the chromatography slice size was  $100 \text{ mm} \times 100 \text{ mm}$ , and the chromatography experiment was

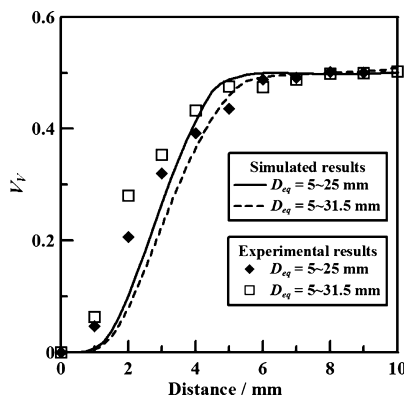


Figure 13. Comparison of the simulated and experimental<sup>76</sup> results for  $V_V$ .

from the boundary of the concrete to a depth of 10 mm. Thus, using these parameters from the experiments of Yang and Yan<sup>76</sup> and eq 26, the experiments for polydisperse cubic aggregate particles were simulated by the present methodology. Figure 13 displays comparisons of the results simulated by the present methodology with the experimental results of Yang et al.<sup>76</sup> As expected, the simulated results are almost agreement with the experimental results from Yang a,<sup>76</sup> and Yans shown in Figure 13. This suggests that the reliability of the results for  $V_V$  simulated by the present methodology is favorable.

Figure 12b,c shows that, for the same PSD and  $V_{\text{agg}}$ , the statistical results for  $S_V$  and  $\lambda^{-3}$  fall in the order cubic particle packing system > octahedral particle packing system > prolate ( $\kappa = 2.5$ ) ellipsoidal particle packing system > dodecahedral particle packing system > icosahedral particle packing system > oblate ( $\kappa = 0.7$ ) ellipsoidal particle packing system > spherical particle packing system. In other words, the two configuration parameters decrease with increasing  $s$ , which is consistent with the results for the monodisperse particle packing structures. This means that the global bond strength of cementitious materials decreases with increasing  $s$ . Similarly, to verify the reliability of the statistical results for  $S_V$  and  $\lambda^{-3}$  for the polydisperse particle packing structures, the theoretical results for  $S_V$  and  $\lambda^{-3}$  for such structures were obtained analogously to the method demonstrated in section 5.2. On the base of preliminary research,<sup>17,18</sup>  $S_V$  is expressed as

$$S_V = \frac{V_{\text{agg}} \langle S \rangle}{\langle V \rangle} \quad (27)$$

where  $\langle V \rangle$  and  $\langle S \rangle$  are the average volume and the average surface area of the aggregate particles, respectively. According to quantitative stereology,<sup>67</sup>  $\langle V \rangle$  and  $\langle S \rangle$  can be written as

$$\langle V \rangle = \int_{D_{\min}}^{D_{\max}} V(D_{\text{eq}}) f_N(D_{\text{eq}}) dD_{\text{eq}} \quad (28)$$

$$\langle S \rangle = \int_{D_{\min}}^{D_{\max}} S(D_{\text{eq}}) f_N(D_{\text{eq}}) dD_{\text{eq}} \quad (29)$$

where  $f_N(D_{\text{eq}})$  is the number-based probability density function for a distribution of nonspherical particles, such as the PPSD (as described in eq 26). Thus, substituting eqs 21, 22, 26, 28,

and 29 into eq 27, the theoretical results for  $S_V$  and  $\lambda^{-3}$  for polydisperse particle packing structures with PPSD can be derived from the equations

$$S_V = \frac{6V_{\text{agg}}}{sD_{\max \text{ eq}}^{0.5} D_{\min \text{ eq}}^{0.5}} \quad (30)$$

$$\lambda^{-3} = \left[ \frac{2s(1 - V_{\text{agg}}) D_{\max \text{ eq}}^{0.5} D_{\min \text{ eq}}^{0.5}}{3V_{\text{agg}}} \right]^{-3} \quad (31)$$

Substitution into eqs 30 and 31 of the initial parameters for each model structure, such as  $D_{\min \text{ eq}} = 5 \text{ mm}$ ,  $D_{\max \text{ eq}} = 45 \text{ mm}$ , and  $V_{\text{agg}} = 0.42$ , gives the theoretical results for  $S_V$  and  $\lambda^{-3}$  with various  $s$  values reported in Table 3. Table 3 compares the

Table 3. Comparison of the Theoretical and Simulated Results for  $S_V$  and  $\lambda^{-3}$  for the Random Packing of Polydisperse Particles with Different  $s$  Values

$(S_V, \lambda^{-3})$			
$s$		statistical results	theoretical results
0.806	cube	$(0.21 \pm 5 \times 10^{-3}, 0.0009 \pm 1 \times 10^{-5})$	$(0.209, 0.00082)$
0.845	octahedron	$(0.20 \pm 7 \times 10^{-3}, 0.0008 \pm 1 \times 10^{-5})$	$(0.198, 0.00071)$
0.885	$\kappa = 2.5$	$(0.20 \pm 1 \times 10^{-3}, 0.0006 \pm 8 \times 10^{-5})$	$(0.190, 0.00062)$
0.910	dodecahedron	$(0.19 \pm 2 \times 10^{-3}, 0.0006 \pm 2 \times 10^{-5})$	$(0.184, 0.00057)$
0.939	icosahedron	$(0.18 \pm 7 \times 10^{-3}, 0.0005 \pm 8 \times 10^{-5})$	$(0.179, 0.00052)$
0.977	$\kappa = 0.7$	$(0.18 \pm 2 \times 10^{-3}, 0.0005 \pm 2 \times 10^{-5})$	$(0.172, 0.00046)$
1	sphere	$(0.17 \pm 4 \times 10^{-3}, 0.0004 \pm 6 \times 10^{-5})$	$(0.168, 0.00043)$

theoretical and statistical results for  $S_V$  and  $\lambda^{-3}$  at different values of  $s$ . It can be seen that the statistical results for  $S_V$  and  $\lambda^{-3}$  present good agreement with the theoretical results for the polydisperse particle packing structures. Moreover, from Table 3, the theoretical results for  $S_V$  and  $\lambda^{-3}$  decrease with increasing  $s$ , consistent with the statistical results, as shown in Figure 12b,c. Therefore, the reliability of the statistical results for  $S_V$  and  $\lambda^{-3}$  for polydisperse particle packing structures is favorable.

## 6. CONCLUSIONS

In this study, random packing models of the mono-/polydisperse convex polyhedral particles have been developed using the presented interparticle overlapping detection algorithm, geometrical algorithm for detecting particle-to-container wall intersection, and random sequential packing algorithm. Compared with the literature, the overlapping detection algorithm displayed favorable accuracy and efficiency. To validate the reliability of the mono-/polydisperse convex polyhedral particle packing models, the sectioning analysis algorithm was presented to derive the sectioning morphology characteristics of these particle packing structures. On the basis of quantitative stereology and the sectioning analysis algorithm, mesostructure models composed of the mono-/polydisperse particles were quantitatively characterized. Furthermore, the influence of particle shape (including cubic, octahedral, dodecahedral, icosahedral, prolate ellipsoidal, oblate ellipsoidal, and spherical) on the configuration parameters of the mesostructure, such as the

volume fraction  $V_V$ , specific surface area  $S_V$ , and third power of the mean free spacing  $\lambda^{-3}$  of the solid phase, was evaluated. The simulated results revealed that the effect of particle shape on the configuration parameter  $V_V$  is weak, irrespective of the mono-/polydisperse particle packing systems. On the other hand, for the mono-/polydisperse particle packing structures, the configuration parameters  $S_V$  and  $\lambda^{-3}$  decrease with increasing sphericity  $s$ . This suggests that the global bond strength of cementitious materials decreases with increasing  $s$ . Moreover, the simulated results were validated by theoretical results, which suggest favorable reliabilities of the proposed methodologies and results.

## APPENDIX A: VERTICES, EDGES, AND FACES OF THE PLATONIC PARTICLES

Here, the size parameter of the Platonic particles is defined as the radius ( $r$ ) of the circumscribed sphere. The origin of the coordinate system  $O'-xyz$  is set as the centroid of the Platonic particles, and the  $z$  axis of the coordinate system is considered to pass through one of vertices, as shown in Figure 2. Thus, the vertices ( $\mathbf{P}_v$ ), edges ( $\mathbf{S}_e$ ), and faces ( $\mathbf{F}_a$ ) of the Platonic particles can be obtained.

For a tetrahedron, there are four vertices ( $v = 1, \dots, 4$ ), six edges ( $e = 1, \dots, 6$ ), and four triangular faces ( $a = 1, \dots, 4$ ). The four vertices  $\mathbf{P}_v$  of the tetrahedron are written as

$$\begin{aligned}\mathbf{P}_1 &= (0, 0, r)^T, & \mathbf{P}_2 &= \left(-\frac{\sqrt{2}}{3}r, \frac{\sqrt{6}}{3}r, -\frac{1}{3}r\right)^T, \\ \mathbf{P}_3 &= \left(-\frac{\sqrt{2}}{3}r, -\frac{\sqrt{6}}{3}r, -\frac{1}{3}r\right)^T, \\ \mathbf{P}_4 &= \left(\frac{2\sqrt{2}}{3}r, 0, -\frac{1}{3}r\right)^T\end{aligned}\quad (\text{A1})$$

where the superscript T denotes the transpose of a vector. According to the four vertices, the six edges  $\mathbf{S}_e$  of the tetrahedron are given by

$$\begin{aligned}\mathbf{S}_1 &= [\mathbf{P}_1, \mathbf{P}_2], & \mathbf{S}_2 &= [\mathbf{P}_1, \mathbf{P}_3], & \mathbf{S}_3 &= [\mathbf{P}_1, \mathbf{P}_4], \\ \mathbf{S}_4 &= [\mathbf{P}_2, \mathbf{P}_3], & \mathbf{S}_5 &= [\mathbf{P}_3, \mathbf{P}_4], & \mathbf{S}_6 &= [\mathbf{P}_4, \mathbf{P}_2]\end{aligned}\quad (\text{A2})$$

where square brackets indicate the subtraction of two vectors. Moreover, on the basis of  $\mathbf{P}_v$ , the four triangular faces  $\mathbf{F}_a$  of the tetrahedron can be expressed as

$$\begin{aligned}\mathbf{F}_1 &= \{\mathbf{P}_1, \mathbf{P}_3, \mathbf{P}_2\}, & \mathbf{F}_2 &= \{\mathbf{P}_1, \mathbf{P}_2, \mathbf{P}_4\}, \\ \mathbf{F}_3 &= \{\mathbf{P}_1, \mathbf{P}_4, \mathbf{P}_3\}, & \mathbf{F}_4 &= \{\mathbf{P}_2, \mathbf{P}_3, \mathbf{P}_4\}\end{aligned}\quad (\text{A3})$$

where braces represent the assembly of vectors. It is worth noting that these vertex vectors comprising each face are arranged in counterclockwise order.

A cube has eight vertices ( $v = 1, \dots, 8$ ), 12 edges ( $e = 1, \dots, 12$ ), and six square faces ( $a = 1, \dots, 6$ ). The eight vertices  $\mathbf{P}_v$  of the cube are denoted as

$$\begin{aligned}\mathbf{P}_1 &= (0, 0, r)^T, & \mathbf{P}_2 &= \left(\frac{2\sqrt{2}}{3}r, 0, \frac{r}{3}\right)^T, \\ \mathbf{P}_3 &= \left(\frac{-\sqrt{2}}{3}r, \frac{\sqrt{6}}{3}r, \frac{r}{3}\right)^T, \\ \mathbf{P}_4 &= \left(\frac{-\sqrt{2}}{3}r, -\frac{\sqrt{6}}{3}r, \frac{r}{3}\right)^T, & \mathbf{P}_5 &= (0, 0, -r)^T, \\ \mathbf{P}_6 &= \left(\frac{-2\sqrt{2}}{3}r, 0, -\frac{r}{3}\right)^T, \\ \mathbf{P}_7 &= \left(\frac{\sqrt{2}}{3}r, -\frac{\sqrt{6}}{3}r, -\frac{r}{3}\right)^T, \\ \mathbf{P}_8 &= \left(\frac{\sqrt{2}}{3}r, \frac{\sqrt{6}}{3}r, -\frac{r}{3}\right)^T\end{aligned}\quad (\text{A4})$$

The six square faces  $\mathbf{F}_a$  of the cube are given by

$$\begin{aligned}\mathbf{F}_1 &= \{\mathbf{P}_1, \mathbf{P}_2, \mathbf{P}_8, \mathbf{P}_3\}, & \mathbf{F}_2 &= \{\mathbf{P}_1, \mathbf{P}_3, \mathbf{P}_6, \mathbf{P}_4\}, \\ \mathbf{F}_3 &= \{\mathbf{P}_1, \mathbf{P}_4, \mathbf{P}_7, \mathbf{P}_2\}, & \mathbf{F}_4 &= \{\mathbf{P}_5, \mathbf{P}_7, \mathbf{P}_4, \mathbf{P}_6\}, \\ \mathbf{F}_5 &= \{\mathbf{P}_5, \mathbf{P}_8, \mathbf{P}_2, \mathbf{P}_7\}, & \mathbf{F}_6 &= \{\mathbf{P}_5, \mathbf{P}_6, \mathbf{P}_3, \mathbf{P}_8\}\end{aligned}\quad (\text{A5})$$

where the connection of neighboring vertices consists of one edge of the particle.

For an octahedron, there are six vertices ( $v = 1, \dots, 6$ ), 12 edges ( $e = 1, \dots, 12$ ), and eight triangular faces ( $a = 1, \dots, 8$ ). The six vertices  $\mathbf{P}_v$  of the octahedron are written as

$$\begin{aligned}\mathbf{P}_1 &= (0, 0, r)^T, & \mathbf{P}_2 &= (0, 0, -r)^T, \\ \mathbf{P}_3 &= \left(\frac{\sqrt{2}}{2}r, -\frac{\sqrt{2}}{2}r, 0\right)^T, & \mathbf{P}_4 &= \left(\frac{\sqrt{2}}{2}r, \frac{\sqrt{2}}{2}r, 0\right)^T, \\ \mathbf{P}_5 &= \left(\frac{-\sqrt{2}}{2}r, \frac{\sqrt{2}}{2}r, 0\right)^T, \\ \mathbf{P}_6 &= \left(\frac{-\sqrt{2}}{2}r, -\frac{\sqrt{2}}{2}r, 0\right)^T\end{aligned}\quad (\text{A6})$$

The eight triangular faces  $\mathbf{F}_a$  of the octahedron are given by

$$\begin{aligned}\mathbf{F}_1 &= \{\mathbf{P}_1, \mathbf{P}_2, \mathbf{P}_3\}, & \mathbf{F}_2 &= \{\mathbf{P}_1, \mathbf{P}_3, \mathbf{P}_4\}, \\ \mathbf{F}_3 &= \{\mathbf{P}_1, \mathbf{P}_4, \mathbf{P}_5\}, & \mathbf{F}_4 &= \{\mathbf{P}_1, \mathbf{P}_5, \mathbf{P}_2\}, \\ \mathbf{F}_5 &= \{\mathbf{P}_6, \mathbf{P}_3, \mathbf{P}_2\}, & \mathbf{F}_6 &= \{\mathbf{P}_6, \mathbf{P}_4, \mathbf{P}_3\}, \\ \mathbf{F}_7 &= \{\mathbf{P}_6, \mathbf{P}_5, \mathbf{P}_4\}, & \mathbf{F}_8 &= \{\mathbf{P}_6, \mathbf{P}_2, \mathbf{P}_3\}\end{aligned}\quad (\text{A7})$$

where the connection of neighboring vertices comprises one edge of the particle.

A dodecahedron has 20 vertices ( $v = 1, \dots, 20$ ), 30 edges ( $e = 1, \dots, 30$ ), and 12 pentagonal faces ( $a = 1, \dots, 12$ ). The 20 vertices  $\mathbf{P}_v$  of the dodecahedron are given by

$$\begin{aligned}
\mathbf{P}_1 &= (0, 0, r)^T, \quad \mathbf{P}_2 = \left( \frac{2r}{3}, 0, \frac{\sqrt{5}r}{3} \right)^T, \\
\mathbf{P}_3 &= \left( \frac{-r}{3}, \frac{\sqrt{3}r}{3}, \frac{\sqrt{5}r}{3} \right)^T, \quad \mathbf{P}_4 = \left( \frac{-r}{3}, \frac{-\sqrt{3}r}{3}, \frac{\sqrt{5}r}{3} \right)^T, \\
\mathbf{P}_5 &= \left( \frac{\sqrt{5}r}{3}, \frac{\sqrt{3}r}{3}, \frac{r}{3} \right)^T, \\
\mathbf{P}_6 &= \left( \frac{3 - \sqrt{5}}{6}r, \frac{\sqrt{15} + \sqrt{3}}{6}r, \frac{r}{3} \right)^T, \\
\mathbf{P}_7 &= \left( \frac{-3 + \sqrt{5}}{6}r, \frac{\sqrt{15} - \sqrt{3}}{6}r, \frac{r}{3} \right)^T, \\
\mathbf{P}_8 &= \left( \frac{-3 + \sqrt{5}}{6}r, -\frac{\sqrt{15} - \sqrt{3}}{6}r, \frac{r}{3} \right)^T, \\
\mathbf{P}_9 &= \left( \frac{3 - \sqrt{5}}{6}r, -\frac{\sqrt{15} + \sqrt{3}}{6}r, \frac{r}{3} \right)^T, \\
\mathbf{P}_{10} &= \left( \frac{\sqrt{5}r}{3}, -\frac{\sqrt{3}r}{3}, \frac{r}{3} \right)^T, \quad \mathbf{P}_{11} = (0, 0, -r)^T, \\
\mathbf{P}_{12} &= \left( \frac{-2r}{3}, 0, -\frac{\sqrt{5}r}{3} \right)^T, \quad \mathbf{P}_{13} = \left( \frac{r}{3}, -\frac{\sqrt{3}r}{3}, -\frac{\sqrt{5}r}{3} \right)^T, \\
\mathbf{P}_{14} &= \left( \frac{r}{3}, \frac{\sqrt{3}r}{3}, -\frac{\sqrt{5}r}{3} \right)^T, \\
\mathbf{P}_{15} &= \left( \frac{-\sqrt{5}r}{3}, \frac{-\sqrt{3}r}{3}, \frac{-r}{3} \right)^T, \\
\mathbf{P}_{16} &= \left( \frac{-3 - \sqrt{5}}{6}r, -\frac{\sqrt{15} + \sqrt{3}}{6}r, \frac{-r}{3} \right)^T, \\
\mathbf{P}_{17} &= \left( \frac{3 + \sqrt{5}}{6}r, -\frac{\sqrt{15} - \sqrt{3}}{6}r, \frac{-r}{3} \right)^T, \\
\mathbf{P}_{18} &= \left( \frac{3 + \sqrt{5}}{6}r, \frac{\sqrt{15} - \sqrt{3}}{6}r, \frac{-r}{3} \right)^T, \\
\mathbf{P}_{19} &= \left( \frac{-3 - \sqrt{5}}{6}r, \frac{\sqrt{15} + \sqrt{3}}{6}r, \frac{-r}{3} \right)^T, \\
\mathbf{P}_{20} &= \left( \frac{-\sqrt{5}r}{3}, \frac{\sqrt{3}r}{3}, \frac{-r}{3} \right)^T
\end{aligned} \tag{A8}$$

The 12 pentagonal faces  $\mathbf{F}_a$  of the dodecahedron are given by

$$\begin{aligned}
\mathbf{F}_1 &= \{\mathbf{P}_1, \mathbf{P}_2, \mathbf{P}_5, \mathbf{P}_6, \mathbf{P}_3\}, \quad \mathbf{F}_2 = \{\mathbf{P}_1, \mathbf{P}_3, \mathbf{P}_7, \mathbf{P}_8, \mathbf{P}_4\}, \\
\mathbf{F}_3 &= \{\mathbf{P}_1, \mathbf{P}_4, \mathbf{P}_9, \mathbf{P}_{10}, \mathbf{P}_2\}, \quad \mathbf{F}_4 = \{\mathbf{P}_2, \mathbf{P}_{10}, \mathbf{P}_{17}, \mathbf{P}_{18}, \mathbf{P}_5\}, \\
\mathbf{F}_5 &= \{\mathbf{P}_3, \mathbf{P}_6, \mathbf{P}_{19}, \mathbf{P}_{20}, \mathbf{P}_7\}, \quad \mathbf{F}_6 = \{\mathbf{P}_4, \mathbf{P}_8, \mathbf{P}_{15}, \mathbf{P}_{16}, \mathbf{P}_9\}, \\
\mathbf{F}_7 &= \{\mathbf{P}_{11}, \mathbf{P}_{13}, \mathbf{P}_{16}, \mathbf{P}_{15}, \mathbf{P}_{12}\}, \\
\mathbf{F}_8 &= \{\mathbf{P}_{11}, \mathbf{P}_{14}, \mathbf{P}_{18}, \mathbf{P}_{17}, \mathbf{P}_{13}\}, \\
\mathbf{F}_9 &= \{\mathbf{P}_{11}, \mathbf{P}_{12}, \mathbf{P}_{20}, \mathbf{P}_{19}, \mathbf{P}_{14}\}, \\
\mathbf{F}_{10} &= \{\mathbf{P}_{12}, \mathbf{P}_{15}, \mathbf{P}_8, \mathbf{P}_7, \mathbf{P}_{20}\}, \\
\mathbf{F}_{11} &= \{\mathbf{P}_{13}, \mathbf{P}_{17}, \mathbf{P}_{10}, \mathbf{P}_9, \mathbf{P}_{16}\}, \\
\mathbf{F}_{12} &= \{\mathbf{P}_{14}, \mathbf{P}_{19}, \mathbf{P}_6, \mathbf{P}_5, \mathbf{P}_{18}\}
\end{aligned} \tag{A9}$$

where the connection of neighboring vertices comprises one edge of the particle.

An icosahedron has 12 vertices ( $v = 1, \dots, 12$ ), 30 edges ( $e = 1, \dots, 30$ ), and 20 triangular faces ( $a = 1, \dots, 20$ ). The 12 vertices  $\mathbf{P}_v$  of the dodecahedron can be written as

$$\begin{aligned}
\mathbf{P}_1 &= (0, 0, r)^T, \quad \mathbf{P}_2 = \left( \frac{2r}{\sqrt{5}}, 0, \frac{r}{\sqrt{5}} \right)^T, \\
\mathbf{P}_3 &= \left( \frac{\sqrt{5} - 1}{2\sqrt{5}}r, \sqrt{\frac{\sqrt{5} + 1}{2\sqrt{5}}}r, \frac{r}{\sqrt{5}} \right)^T, \\
\mathbf{P}_4 &= \left( -\frac{\sqrt{5} + 1}{2\sqrt{5}}r, \sqrt{\frac{\sqrt{5} - 1}{2\sqrt{5}}}r, \frac{r}{\sqrt{5}} \right)^T, \\
\mathbf{P}_5 &= \left( -\frac{\sqrt{5} + 1}{2\sqrt{5}}r, -\sqrt{\frac{\sqrt{5} - 1}{2\sqrt{5}}}r, \frac{r}{\sqrt{5}} \right)^T, \\
\mathbf{P}_6 &= \left( \frac{\sqrt{5} - 1}{2\sqrt{5}}r, -\sqrt{\frac{\sqrt{5} + 1}{2\sqrt{5}}}r, \frac{r}{\sqrt{5}} \right)^T, \\
\mathbf{P}_7 &= (0, 0, -r)^T, \quad \mathbf{P}_8 = \left( -\frac{2r}{\sqrt{5}}, 0, \frac{-r}{\sqrt{5}} \right)^T, \\
\mathbf{P}_9 &= \left( -\frac{\sqrt{5} - 1}{2\sqrt{5}}r, -\sqrt{\frac{\sqrt{5} + 1}{2\sqrt{5}}}r, \frac{-r}{\sqrt{5}} \right)^T, \\
\mathbf{P}_{10} &= \left( \frac{\sqrt{5} + 1}{2\sqrt{5}}r, -\sqrt{\frac{\sqrt{5} - 1}{2\sqrt{5}}}r, \frac{-r}{\sqrt{5}} \right)^T, \\
\mathbf{P}_{11} &= \left( \frac{\sqrt{5} + 1}{2\sqrt{5}}r, \sqrt{\frac{\sqrt{5} - 1}{2\sqrt{5}}}r, \frac{-r}{\sqrt{5}} \right)^T, \\
\mathbf{P}_{12} &= \left( -\frac{\sqrt{5} - 1}{2\sqrt{5}}r, \sqrt{\frac{\sqrt{5} + 1}{2\sqrt{5}}}r, \frac{-r}{\sqrt{5}} \right)^T
\end{aligned} \tag{A10}$$

The 20 triangular faces  $\mathbf{F}_a$  of the icosahedron can be expressed as

$$\begin{aligned}
\mathbf{F}_1 &= \{\mathbf{P}_1, \mathbf{P}_2, \mathbf{P}_3\}, \quad \mathbf{F}_2 = \{\mathbf{P}_1, \mathbf{P}_3, \mathbf{P}_4\}, \\
\mathbf{F}_3 &= \{\mathbf{P}_1, \mathbf{P}_4, \mathbf{P}_5\}, \quad \mathbf{F}_4 = \{\mathbf{P}_1, \mathbf{P}_5, \mathbf{P}_6\}, \\
\mathbf{F}_5 &= \{\mathbf{P}_1, \mathbf{P}_6, \mathbf{P}_2\}, \quad \mathbf{F}_6 = \{\mathbf{P}_2, \mathbf{P}_{11}, \mathbf{P}_3\}, \\
\mathbf{F}_7 &= \{\mathbf{P}_3, \mathbf{P}_{12}, \mathbf{P}_4\}, \quad \mathbf{F}_8 = \{\mathbf{P}_4, \mathbf{P}_8, \mathbf{P}_5\}, \\
\mathbf{F}_9 &= \{\mathbf{P}_5, \mathbf{P}_9, \mathbf{P}_6\}, \quad \mathbf{F}_{10} = \{\mathbf{P}_6, \mathbf{P}_{10}, \mathbf{P}_2\}, \\
\mathbf{F}_{11} &= \{\mathbf{P}_7, \mathbf{P}_9, \mathbf{P}_8\}, \quad \mathbf{F}_{12} = \{\mathbf{P}_7, \mathbf{P}_{10}, \mathbf{P}_9\}, \\
\mathbf{F}_{13} &= \{\mathbf{P}_7, \mathbf{P}_{11}, \mathbf{P}_{10}\}, \quad \mathbf{F}_{14} = \{\mathbf{P}_7, \mathbf{P}_{12}, \mathbf{P}_{11}\}, \\
\mathbf{F}_{15} &= \{\mathbf{P}_7, \mathbf{P}_8, \mathbf{P}_{12}\}, \quad \mathbf{F}_{16} = \{\mathbf{P}_8, \mathbf{P}_9, \mathbf{P}_5\}, \\
\mathbf{F}_{17} &= \{\mathbf{P}_9, \mathbf{P}_{10}, \mathbf{P}_6\}, \quad \mathbf{F}_{18} = \{\mathbf{P}_{10}, \mathbf{P}_{11}, \mathbf{P}_2\}, \\
\mathbf{F}_{19} &= \{\mathbf{P}_{11}, \mathbf{P}_{12}, \mathbf{P}_3\}, \quad \mathbf{F}_{20} = \{\mathbf{P}_{12}, \mathbf{P}_8, \mathbf{P}_4\}
\end{aligned} \tag{A11}$$

where the connection of neighboring vertices comprises one edge of the particle.

## APPENDIX B: RELATIONSHIPS BETWEEN THE EQUIVALENT DIAMETER $D_{EQ}$ AND THE SIZE $R$ FOR FIVE PLATONIC PARTICLES

The volume of a tetrahedron is written as

$$V = \frac{8\sqrt{3}}{27}r^3 \tag{B1}$$

Thus, according to the definition of the equivalent diameter, the relationship between the equivalent diameter  $D_{eq}$  and the radius  $r$  of the circumscribed sphere of the tetrahedron is given by

$$r = \frac{\sqrt{6} \sqrt[3]{\pi} \sqrt[3]{2}}{4} D_{eq} \quad (B2)$$

The volume of a cube is given by

$$V = \frac{8\sqrt{3}}{9} r^3 \quad (B3)$$

So, the relationship between  $D_{eq}$  and the size  $r$  of the cube can be written as

$$r = \frac{\sqrt{3} \sqrt[3]{\pi}}{2\sqrt[3]{6}} D_{eq} \quad (B4)$$

The volume of an octahedron is represented by

$$V = \frac{4}{3} r^3 \quad (B5)$$

Thus, the relationship between  $D_{eq}$  and the size  $r$  of the octahedron can be derived as

$$r = \frac{\sqrt[3]{\pi}}{2} D_{eq} \quad (B6)$$

For a dodecahedron, the volume is expressed as

$$V = \frac{2(5 + \sqrt{5})}{3\sqrt{3}} r^3 \quad (B7)$$

Therefore, the relationship between  $D_{eq}$  and the size  $r$  of the dodecahedron can be given by

$$r = \frac{\sqrt[3]{3} \sqrt[3]{\pi(5 - \sqrt{5})}}{2\sqrt[3]{10}} D_{eq} \quad (B8)$$

The volume of an icosahedron is written as

$$V = \frac{2\sqrt{10 + 2\sqrt{5}}}{3} r^3 \quad (B9)$$

Thus, the relationship between  $D_{eq}$  and the size  $r$  of the icosahedron is given by

$$r = \frac{\sqrt[3]{\pi}}{\sqrt[3]{4} \sqrt[3]{10 + 2\sqrt{5}}} D_{eq} \quad (B10)$$

## AUTHOR INFORMATION

### Corresponding Author

\*Tel.: +86-25-52090645. Fax: +86-25-52090667. E-mail: chenhs@seu.edu.cn.

### Notes

The authors declare no competing financial interest.

## ACKNOWLEDGMENTS

The authors greatly appreciate the reviewers' helpful comments for the quality of our article. We also acknowledge financial support from the Ministry of Science and Technology of China "973 Project" (Grant 2009CB623203) and the Scientific Research Foundation of Graduate School of Southeast University (Grant YBJJ1115).

## REFERENCES

- (1) Chen, H. S.; Sun, W.; Stroeven, P.; Sluys, L. J. Overestimation of the interface thickness around convex-shaped grain by sectional analysis. *Acta Mater.* **2007**, *55*, 3943.
- (2) Xu, W. X.; Chen, H. S. Analytical and modeling investigations of volume fraction of interfacial layers around ellipsoidal aggregate particles in multiphase materials. *Model. Simul. Mater. Sci. Eng.* **2013**, *21*, 015007.
- (3) Yu, A. B.; Zou, R. P.; Standish, N. Modifying the linear packing model for predicting the porosity of nonspherical particle mixtures. *Ind. Eng. Chem. Res.* **1996**, *35*, 3730.
- (4) Xu, W. X.; Chen, H. S. Numerical investigation of effect of particle shape and particle size distribution on fresh cement paste microstructure via random sequential packing of dodecahedral cement particles. *Comput. Struct.* **2013**, *114–115*, 35.
- (5) Dias, R. P.; Teixeira, J. A.; Mota, M. G.; Yelshin, A. I. Particulate binary mixtures: Dependence of packing porosity on particle size ratio. *Ind. Eng. Chem. Res.* **2004**, *43*, 7912.
- (6) Wang, M.; Pan, N. Predictions of effective physical properties of complex multiphase materials. *Mater. Sci. Eng. R* **2008**, *63*, 1.
- (7) Rao, M. S.; Toor, H. L. Heat transfer from a particle to a surrounding bed of particles. Effect of size and conductivity ratios. *Ind. Eng. Chem. Res.* **1987**, *26*, 469.
- (8) tSaoir, M. N. A.; Fernandes, D. L. A.; Sá, J.; Kitagawa, K.; Hardacre, C.; Aiouache, F. Three-dimensional water vapor visualization in porous packing by near-infrared diffuse transmittance tomography. *Ind. Eng. Chem. Res.* **2012**, *51*, 8875.
- (9) Stroeven, P.; Guo, Z. Q. Modern perspectives on aggregate in concrete. In *Advances in Construction Materials*; Grosse, C. U., Ed.; Springer-Verlag: New York, 2007; p 757.
- (10) Latham, J. P.; Munjiza, A. The modeling of particle systems with real shapes. *Philos. Trans. R. Soc. A* **2004**, *362*, 1953.
- (11) Garboczi, E. J.; Bullard, J. W. Shape analysis of a reference cement. *Cem. Concr. Res.* **2004**, *34*, 1933.
- (12) Jia, X.; Gan, M.; Williams, R. A.; Rhodes, D. Validation of a digital packing algorithm in predicting powder packing densities. *Powder Technol.* **2007**, *174*, 10.
- (13) Green, C. W.; Farone, J.; Briley, J. K.; Eldridge, R. B.; Ketcham, R. A.; Nightingale, B. Novel application of X-ray computed tomography: Determination of gas/liquid contact area and liquid holdup in structured packing. *Ind. Eng. Chem. Res.* **2007**, *46*, 5734.
- (14) Owens, S. A.; Kossmann, A.; Farone, J.; Eldridge, R. B.; Ketcham, R. A. Flow field visualization in structured packing using real time X-ray radiography. *Ind. Eng. Chem. Res.* **2009**, *48*, 3606.
- (15) Gélinas, V.; Vidal, D. Determination of particle shape distribution of clay using an automated AFM image analysis method. *Powder Technol.* **2010**, *203*, 254.
- (16) Xu, W. X.; Chen, H. S.; Lv, Z. An overlapping detection algorithm for random sequential packing of elliptical particles. *Physica A* **2011**, *390*, 2452.
- (17) Xu, W. X.; Chen, H. S. Mesoscale characterization of particulate composites via a contact detection algorithm of ellipsoidal particles. *Powder Technol.* **2012**, *221*, 296.
- (18) Xu, W. X.; Chen, H. S. Microstructural characterization of fresh cement paste via random packing of ellipsoidal cement particles. *Mater. Charact.* **2012**, *66*, 16.
- (19) Cundall, P. A.; Strack, O. D. L. A discrete numerical model for granular assemblies. *Géotechnique* **1979**, *29*, 47.
- (20) Zhu, H. P.; Zhou, Z. Y.; Yang, R. Y.; Yu, A. B. Discrete particle simulation of particulate systems: Theoretical developments. *Chem. Eng. Sci.* **2007**, *62*, 3378.
- (21) Beham, M.; Dixon, A. G.; Nijemeisland, M.; Stitt, E. H. Catalyst deactivation in 3D CFD resolved particle simulations of propane dehydrogenation. *Ind. Eng. Chem. Res.* **2010**, *49*, 10641.
- (22) Benyahia, S.; Galvin, J. E. Estimation of numerical errors related to some basic assumptions in discrete particle methods. *Ind. Eng. Chem. Res.* **2010**, *49*, 10588.
- (23) Yi, L. Y.; Dong, K. J.; Zou, R. P.; Yu, A. B. Coordination number of the packing of ternary mixtures of spheres: DEM simulations versus measurements. *Ind. Eng. Chem. Res.* **2011**, *50*, 8773.

- (24) Jayasundara, C. T.; Yang, R. Y.; Yu, A. B. Discrete particle simulation of particle flow in a stirred mill: Effect of mill properties and geometry. *Ind. Eng. Chem. Res.* **2012**, *51*, 1050.
- (25) Lubachevsky, B. D.; Stillinger, F. H. Geometric properties of random disk packings. *J. Stat. Phys.* **1990**, *60*, 561.
- (26) Donev, A.; Cisse, I.; Sachs, D.; Variano, E. A.; Stillinger, F. H.; Connelly, R.; Torquato, S.; Chaikin, P. M. Improving the density of jammed disordered packings using ellipsoids. *Science* **2004**, *303*, 990.
- (27) Donev, A.; Torquato, S.; Stillinger, F. H. Neighbor list collision-driven molecular dynamics simulation for nonspherical hard particles. I. Algorithmic details. *J. Comput. Phys.* **2005**, *202*, 737.
- (28) Chaikin, P. M.; Donev, A.; Man, W.; Stillinger, F. H.; Torquato, S. Some observations on the random packing of hard ellipsoids. *Ind. Eng. Chem. Res.* **2006**, *45*, 6960.
- (29) He, D.; Ekere, N. N.; Cai, L. Computer simulation of random packing of unequal particles. *Phys. Rev. E* **1999**, *60*, 7098.
- (30) Zhao, J.; Li, S. X.; Lu, P.; Meng, L. Y.; Li, T.; Zhu, H. P. Shape influences on the packing density of frustums. *Powder Technol.* **2011**, *214*, 500.
- (31) Zhao, J.; Li, S. X.; Zou, R. P.; Yu, A. B. Dense random packings of spherocylinders. *Soft Matter* **2012**, *8*, 1003.
- (32) Williams, S. R.; Philipse, A. P. Random packings of spheres and spherocylinders simulated by mechanical contraction. *Phys. Rev. E* **2003**, *67*, 051301.
- (33) Wouterse, A.; Williams, S. R.; Philipse, A. P. Effect of particle shape on the density and microstructure of random packings. *J. Phys.: Condens. Matter* **2007**, *19*, 406215.
- (34) Lee, Y.; Yang, C. T.; Chien, C. S. A 3D ellipsoid-based model for packing of granular particles. *Int. J. Comput. Appl. Technol.* **2003**, *17*, 148.
- (35) Lee, Y.; Fang, C.; Tsou, Y. R.; Lu, L. S.; Yang, C. T. A packing algorithm for three-dimensional convex particles. *Granular Matter* **2009**, *11*, 307.
- (36) Yu, Y.; Cui, J. Z.; Han, F. An effective computer generation method for the composites with random distribution of large numbers of heterogeneous grains. *Compos. Sci. Technol.* **2008**, *68*, 2543.
- (37) Sobolev, K.; Amirjanov, A. The development of a simulation model of the dense packing of large particulate assemblies. *Powder Technol.* **2004**, *141*, 155.
- (38) Torquato, S.; Jiao, Y. Dense packings of polyhedral: Platonic and Archimedean solids. *Phys. Rev. E* **2009**, *80*, 044110.
- (39) Torquato, S.; Jiao, Y. Dense packings of the Platonic and Archimedean solids. *Nature* **2009**, *460*, 876.
- (40) Baker, J.; Kudrolli, A. Maximum and minimum stable random packings of Platonic solids. *Phys. Rev. E* **2010**, *82*, 061304.
- (41) Agarwal, U.; Escobedo, F. A. Mesophase behavior of polyhedral particles. *Nat. Mater.* **2011**, *10*, 230.
- (42) Henzie, J.; Grünwald, M.; Widmer-Cooper, A.; Geissler, P. L.; Yang, P. D. Self-assembly of uniform polyhedral silver nanocrystals into densest packings and exotic superlattices. *Nat. Mater.* **2012**, *11*, 131.
- (43) Roskilly, S. J.; Colbourn, E. A.; Alli, O.; Williams, D.; Paul, K. A.; Welfare, E. H.; Trusty, P. A. Investigating the effect of shape on particle segregation using a Monte Carlo simulation. *Powder Technol.* **2010**, *203*, 211.
- (44) Li, S. X.; Zhao, J.; Zhou, X. Numerical simulation of random close packing with tetrahedral. *Chin. Phys. Lett.* **2008**, *25*, 1724.
- (45) Jiménez, J. J.; Segura, R. J. Collision detection between complex polyhedra. *Comput. Graph.* **2008**, *32*, 402.
- (46) Cundall, P. A. Formulation of a three-dimensional discrete element model—Part I. A scheme to detect and represent contacts in a system composed of many polyhedral blocks. *Int. J. Rock Mech. Min. Sci.* **1988**, *25*, 107.
- (47) Nezami, E. G.; Hashash, Y. M. A.; Zhao, D. W.; Ghaboussi, J. A fast contact detection algorithm for 3-D discrete element method. *Comput. Geotech.* **2004**, *31*, 575.
- (48) Nezami, E. G.; Hashash, Y. M. A.; Zhao, D. W.; Ghaboussi, J. Shortest link method for contact detection in discrete element method. *Int. J. Numer. Anal. Methods Geomech.* **2006**, *30*, 783.
- (49) Barbosa, R. E. *Discrete Element Models for Granular Materials and Rock Mass*. Ph.D. Thesis, University of Illinois at Urbana-Champaign, Urbana, IL, 1990.
- (50) Liu, X. L.; Lemos, J. V. Procedure for contact detection in discrete element analysis. *Adv. Eng. Software* **2001**, *32*, 409.
- (51) Jiang, Q. H.; Yeung, M. R. A. model of point-to-face contact for three-dimensional discontinuous deformation analysis. *Rock Mech. Rock Eng.* **2004**, *37*, 95.
- (52) Yeung, M. R.; Jiang, Q. H.; Sun, N. A model of edge-to-edge contact for three-dimensional discontinuous deformation analysis. *Comput. Geotech.* **2007**, *34*, 175.
- (53) Wu, J. H.; Juang, C. H.; Lin, H. M. Vertex-to-face contact searching algorithm for three-dimensional frictionless contact problems. *Int. J. Numer. Methods Eng.* **2005**, *63*, 876.
- (54) Wu, J. H. New edge-to-edge contact calculating algorithm in three-dimensional discrete numerical analysis. *Adv. Eng. Software* **2008**, *39*, 15.
- (55) Ahn, T. Y.; Ryu, S. H.; Song, J. J.; Lee, C. I. A new contact method using inscribed sphere for 3D discontinuous deformation analysis. In *Analysis of Discontinuous Deformation: New Developments and Applications*; Ma, G. W.; Zhou, Y. X., Eds.; Research Publishing Services: Singapore, 2009; p 127.
- (56) Schneider, P.; Eberly, D. H. *Geometric Tools for Computer Graphics*; Morgan Kaufmann: San Francisco, 2003.
- (57) O'Rourke, J.; Chien, C. B.; Olson, T.; Naddor, D. A new linear algorithm for intersecting convex polygons. *Comput. Graph. Image Process.* **1982**, *19*, 384.
- (58) Preparata, F. P.; Shamos, M. I. *Computational Geometry. An Introduction*; Springer: Berlin, 1985.
- (59) Xu, W. X.; Chen, H. S.; Lv, Z. A 2D elliptical model of random packing for aggregates in concrete. *J. Wuhan Univ. Technol., Mater. Sci. Ed.* **2010**, *25*, 717.
- (60) Georgiades, P. Signed distance from point to plane. In *Graphics Gems III*; Kirk, D., Ed.; Academic Press: New York, 1992; p 223.
- (61) Stroeven, P.; He, H.; Guo, Z. Q.; Stroeven, M. Particle packing in a model concrete at different levels of the microstructure: Evidence of an intrinsic patchy nature. *Mater. Charact.* **2009**, *60*, 1088.
- (62) He, H.; Guo, Z. Q.; Stroeven, P.; Stroeven, M.; Sluys, L. J. Characterization of the packing of aggregate in concrete by discrete element approach. *Mater. Charact.* **2009**, *60*, 1082.
- (63) Dolado, J. S.; van Breugel, K. Recent advances in modeling for cementitious materials. *Cem. Concr. Res.* **2011**, *41*, 711.
- (64) Zheng, J. J.; Guo, Z. Q.; Pan, X. D.; Stroeven, P.; Sluys, L. J. ITZ volume fraction in concrete with spheroidal aggregate particles and application: Part I. Numerical algorithm. *Mag. Concr. Res.* **2011**, *63*, 473.
- (65) Chen, H. S.; Sluys, L. J.; Stroeven, P.; Sun, W. Theoretical prediction on thickness distribution of cement paste among neighboring aggregates in concrete. *Comput. Concr.* **2011**, *8*, 163.
- (66) Brak, R.; Guttman, A. J. Exact solution of the staircase and row-convex polygon perimeter and area generating function. *J. Phys. A: Math. Gen.* **1990**, *23*, 4581.
- (67) Underwood, E. E. *Quantitative Stereology*; Addison-Wesley: Boston, 1968.
- (68) Xu, W. X.; Chen, H. S. Quantitative characterization of microstructure of fresh cement paste via random packing of polydispersed Platonic cement particles. *Model. Simul. Mater. Sci. Eng.* **2012**, *20*, 075003.
- (69) Xu, W. X.; Lv, Z.; Chen, H. S. The effects of particle size distribution, shape and volume fraction of aggregates on the wall effect of concrete via random sequential packing of polydispersed spheroidal particles. *Physica A* **2013**, *392*, 416.
- (70) Stroeven, P.; Hu, J. Gradient structure in cementitious materials. *Cem. Concr. Comp.* **2007**, *29*, 313.
- (71) Splitgerber, H.; Wittmann, F. H. Effect of adsorbed water films on the van der Waals forces between quartz glass surfaces. *Surf. Sci.* **1974**, *41*, 504.
- (72) Brown, G. G. *Unit Operations*; Wiley: New York, 1950.

- (73) Zhou, Z. Y.; Zou, R. P.; Pinson, D.; Yu, A. B. Dynamic simulation of the packing of ellipsoidal particles. *Ind. Eng. Chem. Res.* **2011**, *50*, 9787.
- (74) Zhou, Z. Y.; Pinson, D.; Zou, R. P.; Yu, A. B. Discrete particle simulation of gas fluidization of ellipsoidal particles. *Chem. Eng. Sci.* **2011**, *66*, 6128.
- (75) Zou, R. P.; Yu, A. B. Evaluation of the packing characteristics of mono-sized non-spherical particles. *Powder Technol.* **1996**, *88*, 71.
- (76) Yang, J.; Yan, P. Distribution characteristics of coarse aggregate in wall-affecting layer of concrete. *J. Build. Mater.* **2009**, *12*, 580 (in Chinese).
- (77) Garboczi, E. J.; Bentz, D. Analytical formulas for interfacial transition zone properties. *Adv. Cem. Based Mater.* **1997**, *6*, 99.
- (78) Lu, B. L.; Torquato, S. Nearest-surface distribution functions for polydispersed particle systems. *Phys. Rev. A* **1992**, *45*, 5530.